https://doi.org/10.5194/egusphere-2026-6624
Preprint. Discussion started: 10 November 2026
© Author(s) 2026. CC BY 4.0 License.

The integrated aerosol–climate model CIESM-PAMT: Part 2. Evaluation of clouds, precipitation, radiation, and aerosol–cloud interactions

Hengqi Wang[1,a], Yiran Peng[1*], Knut von Salzen[2,3], Husi Letu[4], Minqi Wang[1,b], Jiangnan Li[3], Hailing Jia[5], Huazhe Shang[4], Dabin Ji[4], Yuying Wang[6], Xin He[7], Luke Fraser-Leach[8], and Johannes Quaas[9]

[1]Department of Earth System Science, Ministry of Education Key Laboratory for Earth System Modeling, Institute for Global Change Studies, Tsinghua University, Beijing, 100084, China
[2]Department of Atmospheric and Climate Science, University of Washington, Washington, Seattle, USA
[3]Canadian Centre for Climate Modelling and Analysis, Environment and Climate Change Canada, Victoria, British Columbia, Canada
[4]State Key Laboratory of Remote Sensing and Digital Earth, Aerospace Information Research Institute, Chinese Academy of Sciences, Beijing, 100094, China
[5]SRON Space Research Organisation Netherlands, Leiden, 2333 CA, Netherlands
[6]State Key Laboratory of Climate System Prediction and Risk Management/Key Laboratory for Aerosol-Cloud Precipitation of China Meteorological Administration/Special Test Field of National Integrated Meteorological Observation, Nanjing University of Information Science and Technology, Nanjing 210044, China
[7]Jiangsu Key Laboratory of Intelligent Atmospheric Environment Monitoring and Carbon–Pollution Co-control, Collaborative Innovation Center of Atmospheric Environment and Equipment Technology, School of Environmental Science and Engineering, Nanjing University of Information Science and Technology, Nanjing 210044, China
[8]Department of Physics, University of Toronto, Toronto, M5S1A7, Canada
[9]Leipzig Institute of Meteorology, Leipzig University, Leipzig, 04109, Germany
[a]now at: State Key Laboratory of Remote Sensing and Digital Earth, Aerospace Information Research Institute, Chinese Academy of Sciences, Beijing, 100094, China
[b]now at: COMNOVA, Shanghai, 201203, China

Correspondence to: Yiran Peng (pyiran@mail.tsinghua.edu.cn)

Abstract. Aerosol–cloud interactions (ACI) remain one of the largest sources of uncertainty in current climate simulations, with their climatic effects strongly dependent on the coupling between aerosols, clouds, and radiation. To improve the physical representation of aerosol processes in the Community Integrated Earth System Model (CIESM), this study couples a new aerosol module, the Piecewise lognormal approximation Aerosol Model for Tsinghua University (PAMT), to construct the integrated aerosol–climate model CIESM-PAMT. In Part 1, we introduced the coupling framework and systematically evaluated its performance in simulating aerosols. Results showed that the new aerosol module PAMT substantially enhanced CIESM's ability to simulate global aerosol optical properties and mass/number concentrations, providing a more reliable foundation for subsequent assessments of aerosol impacts on clouds and radiation.

Building on this, Part 2 uses multi-source observations to further evaluate CIESM-PAMT's performance in simulating clouds, precipitation, radiation, and ACI, with systematic comparison to the original CIESM coupled with the Aerosol Module with seven lognormal modes (CIESM-MAM7). The results indicate that CIESM reproduces clouds, precipitation, and radiation with high fidelity, with simulated values largely falling within observational uncertainty ranges. Specifically, CIESM-PAMT

https://doi.org/10.5194/egusphere-2026-6624
Preprint. Discussion started: 10 November 2026
© Author(s) 2026. CC BY 4.0 License.

shows better performance in simulating cloud condensation nuclei and cloud droplet number concentrations, while CIESM-MAM7 shows slightly better performance in cloud fraction. Both modules perform similarly for cloud droplet effective radius, liquid/ice water paths, and radiation-related variables. In terms of ACI representation, CIESM-PAMT provides a more realistic simulation of the Twomey effect, demonstrating an effective improvement in ACI modeling. These findings further suggest that aerosol impacts on atmospheric composition are primarily mediated through changes in cloud droplet number, with comparatively limited effects on other cloud properties. The study also identifies future avenues for model improvement, including enhanced representation of cloud fraction and hydrometeors, diagnostics and reduction of biases in cloud radiative effects and forcing, clarification of differences arising from alternative microphysical schemes, and expanded investigation of aerosol–ice cloud and aerosol–convective cloud interactions.

Overall, CIESM-PAMT exhibits robust aerosol–cloud–radiation coupling capabilities, providing a reliable platform for probing the physical mechanisms by which aerosols influence the climate system, and laying an important foundation for further model development and participation in international comparison projects.

1 Introduction

Aerosols play a critical role in the Earth's climate system by influencing cloud and radiation processes (Bellouin et al., 2020; IPCC, 2023). They can directly modify the Earth's energy balance by scattering and absorbing solar radiation (aerosol-radiation interactions, ARI). In addition, aerosols can also act as cloud condensation nuclei (CCN) or ice nuclei (IN), modifying cloud droplet number concentration and effective radius, thereby affecting cloud optical properties and adjusting the cloud lifetime (Aerosol–Cloud Interactions, ACI), ultimately influencing climate feedbacks (Albrecht, 1989; Bellouin et al., 2020; Twomey, 1977; Wang et al., 2025a; Yu et al., 2006). However, ACI remains as one of the largest sources of uncertainty in global climate assessments (IPCC, 2023). Reducing this uncertainty is essential for improving the accuracy of climate projections and for better assessing climate feedbacks and risks of extreme weather.

To quantify the impacts of aerosols on the climate system, developing climate models with online-coupled aerosol modules is an effective approach. In Part 1 of this study, we introduced the integrated aerosol–climate model CIESM-PAMT and described its performance in simulating aerosols (Wang et al., Part 1, 2026). The Piecewise lognormal approximation Aerosol Model (PAM) used in AMAP (2021) was further developed and implemented into the Community Integrated Earth System Model (CIESM) (Lin et al., 2020), resulting in an adapted aerosol module hereafter referred to as PAMT (PAM for Tsinghua University). The resulting integrated aerosol–climate model, CIESM-PAMT, effectively simulates multimodal aerosol mass and number concentrations as well as aerosol optical properties, substantially improving the representation of the global aerosol distribution and its spatiotemporal variability. Within the complex cloud microphysical and radiative feedback processes, different aerosol properties can trigger multiscale nonlinear responses in cloud droplet effective radius, liquid water content, precipitation intensity, and cloud albedo (Jia and Quaas, 2023). These changes affect not only the regional energy balance but

https://doi.org/10.5194/egusphere-2026-6624
Preprint. Discussion started: 10 November 2026
© Author(s) 2026. CC BY 4.0 License.

also exert profound influences on global climate feedbacks (Quaas and Gryspeerdt, 2022). Therefore, a systematic evaluation of aerosol–cloud–radiation coupling processes is a critical step for testing and improving model credibility.

In this study (Part 2), we build on the CIESM-PAMT framework and presents a comprehensive evaluation of simulated clouds, precipitation, radiation, and ACI. The evaluation uses a wide range of datasets, including ground-based observations, satellite products, reanalysis data, and multi-model results. Through these analyses, the results provide quantitative evidence of the current model performance and offer guidance for further model development and its future participation in the model intercomparison projects.

The paper is organized as follows. Section 2 briefly introduces the CIESM-PAMT and the experimental design. Section 3 describes the multi-source observational datasets used in this study. Section 4 evaluates the performance of CIESM-PAMT relative to the original aerosol module in simulating cloud properties (including total/high/middle/low/ice/liquid cloud fractions, liquid/ice cloud water paths, cloud droplet effective radius, cloud condensation nuclei, and cloud droplet number concentration), precipitation, radiation (top-of-atmosphere fluxes and cloud radiative effects), and different ACI effects. Finally, Section 5 presents the summary and discussion.

2. Model

2.1 Overview of CIESM-PAMT

The Community Integrated Earth System Model version 1.1 (CIESM) is an Earth system model developed by Tsinghua University and released in 2019 (Lin et al., 2020). It is built upon version 1.2.1 of the Community Earth System Model developed by the National Center for Atmospheric Research (i.e., NCAR CESM1.2.1) (Hurrell et al., 2013), and incorporates 13 independently developed or substantially improved physical parameterizations and modules (Huang et al., 2016; Jin et al., 2011; Liang et al., 2017; Liu et al., 2018; Lüpkes et al., 2012; Qin et al., 2018; Shangguan et al., 2014; Song and Zhang, 2011; Wang et al., 2016; Yang et al., 2008; Zhang and Li, 2013; Zhao et al., 2017). CIESM has participated in multiple model intercomparison projects, including the Coupled Model Intercomparison Project Phase 6 (CMIP6), exhibits satisfactory overall performance (Chin et al., 2026; Lin et al., 2020; von Salzen et al., 2022; Whaley et al., 2022). The original version of CIESM was coupled with the aerosol module with seven lognormal modes (MAM7) (Liu et al., 2012), and the coupled configuration is referred to as CIESM-MAM7. During its participation in CMIP6 experiments, the aerosol–model coupling was turned off, and prescribed aerosol fields were used for climate simulations (Lin et al., 2020; Stevens et al., 2017). Note that the MAM7 framework has undergone further development in subsequent studies (Glotfelty et al., 2017; Ke et al., 2022; Wu et al., 2018; Zaveri et al., 2021) . These developments are not included in the version used in this study, which specifically refers to the MAM7 implementation in CIESM described by Liu et al. (2012).

CIESM-PAMT is a new integrated aerosol–climate model (Wang et al., Part 1, 2026). The objective of this development is to retain the strengths of the original CIESM climate system framework and physical processes, while providing a more detailed

https://doi.org/10.5194/egusphere-2026-6624
Preprint. Discussion started: 10 November 2026
© Author(s) 2026. CC BY 4.0 License.

representation of aerosol processes, thereby enhancing the model's capability to simulate aerosol–cloud–climate processes. The coupling framework is illustrated in Fig. 1.

The PAMT differs substantially from the previously coupled MAM7 in its representation of aerosol size distributions, aerosol mixing states, source–sink process parameterizations, and optical property calculations. Here we provide a brief overview, and more detailed descriptions are presented in Part 1 of this study.

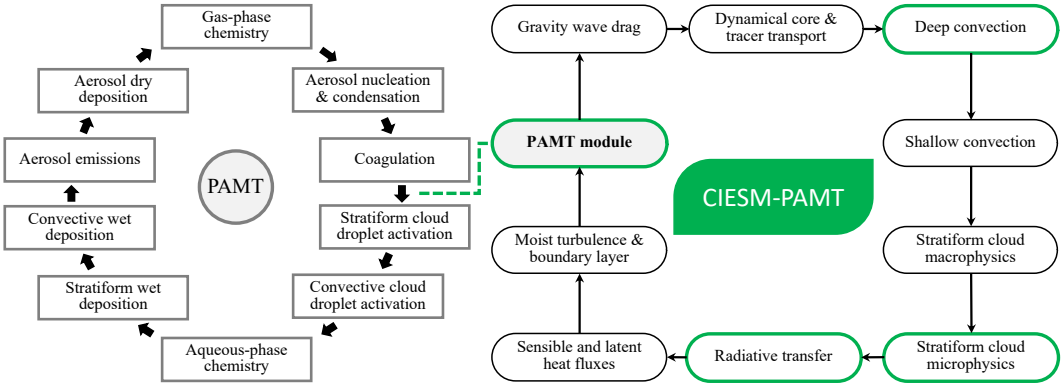


Figure 1. Schematic of online aerosol coupling in CIESM with PAMT. Processes related to aerosols are marked in green.

2.1.1 Size Distributions and Mixing State

PAMT uses the Piecewise Lognormal Approximation (PLA) method (von Salzen, 2006), in which the aerosol size distribution is divided into multiple sections. Within each section, the size distribution is assumed to follow a lognormal form, and the distribution parameters are dynamically updated based on the model-predicted aerosol number/mass concentrations. The PLA method combines the strengths of both the sectional and modal approaches within a unified framework. Compared with the traditional sectional approach, PLA retains a detailed representation of the aerosol size distribution while substantially reducing computational cost; compared with the modal approach, it allows the simulation accuracy to be conveniently controlled by adjusting the number of sections, providing greater flexibility. Thus, the PLA method offers both high accuracy and computational efficiency, making it well-suited for use in climate models. In the current CIESM-PAMT configuration, 9 lognormal sections are used. Sulfate (SO4), part of organic aerosol (OA) and black carbon (BC) are treated as internally mixed, while dust (DU), sea salt (SS), and the remaining BC/OC are treated as externally mixed and represented by separate sections. MAM7 classifies aerosols into seven modes based on particle size distribution and mixing state, including Aitken, accumulation, primary carbon, fine/coarse SS, and fine/coarse DU modes (Liu et al., 2012). Within each mode, the aerosol size distribution is represented by a lognormal distribution.

2.1.2 Sources and Sinks of Aerosols

1) ***Emissions:*** PAMT and MAM7 use the same historical emission inventories from CMIP6 and AeroCom (Hoesly et al., 2018), including sulfur dioxide (SO_2), volatile organic compounds (VOCs), dimethyl sulfide (DMS), primary organic

https://doi.org/10.5194/egusphere-2026-6624
Preprint. Discussion started: 10 November 2026
© Author(s) 2026. CC BY 4.0 License.

aerosol (POA) and BC. The inventories are processed into external forcing fields suitable for model input using procedures similar to those in Neale et al. (2012). Emissions of DU and SS in PAMT are treated with online calculations (Lewis and Schwartz, 2004; Ma et al., 2008; Peng et al., 2012), with emission fluxes calculated based on bare soil fraction, wind speed, soil moisture, and sea surface wind speed. In MAM7, DU and SS emissions are likewise computed online, but the parameterization schemes differ from those implemented in PAMT (Mahowald et al., 2006a, b; Mårtensson et al., 2003; Monahan et al., 1986; Okin, 2008).

2) ***Chemistry:*** PAMT adopts the same gas-phase chemistry as MAM7, including the production and loss of hydrogen peroxide (H_2O_2), the oxidation of SO_2 and DMS, and the formation of sulfuric acid (H_2SO_4) vapor (Emmons et al., 2010). For pH calculations, PAMT accounts for the influence of droplet pH on reaction rates and solves the ion equilibrium equations using an iterative method (von Salzen et al., 2000). In contrast, MAM7 obtains equilibrium values by scanning across a prescribed pH range (Tie et al., 2001).

3) ***Aerosol nucleation:*** PAMT provides three sulfate aerosol nucleation schemes (Dunne et al., 2016; Kulmala et al., 1998; Merikanto et al., 2007). In this study, PAMT adopts the parameterization proposed by Dunne et al. (2016), which considers sulfuric acid, ammonia, organics, water vapor, and galactic cosmic rays, whereas MAM7 uses the scheme developed by Merikanto et al. (2007).

4) ***Condensation and BC aging:*** In PAMT, gaseous H_2SO_4 and VOCs condense onto pre-existing aerosols (e.g., SO4, SS, and OA), modifying their composition and hygroscopicity through the Fuchs–Sutugin equation (Hanson, 2005; Russell et al., 1994; von Salzen, 2006). Hydrophobic BC ages to hydrophilic BC using prescribed daytime (1 h) and nighttime (24 h) e-folding timescales (Croft et al., 2005). In MAM7, H_2SO_4, ammonia (NH_3), and secondary organic aerosol (SOA) condensation is treated dynamically over each aerosol mode using standard mass-transfer theory (Binkowski and Shankar, 1995; Pöschl et al., 1998; Seinfeld and Pandis, 2006). BC aging occurs through sulfate coating, transferring fresh BC to the accumulation mode (Liu et al., 2012).

5) ***Coagulation:*** PAMT parameterizes aerosol coagulation using a piecewise linear representation of the aerosol size distribution with 21 sections (Tzivion et al. (1987); Fraser-Leach et al., in preparation). Coagulation is applied only to internally mixed aerosols, with the kernel calculated assuming Brownian diffusion using Fuchs' interpolation (Seinfeld and Pandis, 2006). In contrast, MAM7 treats coagulation as intermodal number transfer using a simpler numerical scheme adopted from the Community Multiscale Air Quality model (Binkowski and Roselle, 2003).

6) ***Water uptake:*** Both PAMT and MAM7 parameterize aerosol water uptake using Köhler theory (Ghan and Zaveri, 2007; Köhler, 1936). However, PAMT allows the hygroscopicity parameter (κ) to vary with relative humidity based on Aerosol Inorganic Model (AIM) simulations (Wexler and Clegg, 2002), whereas MAM7 assumes constant κ values (Neale et al., 2012; Petters and Kreidenweis, 2007). Both modules account for the effect of size-dependent curvature (Kelvin effect), but PAMT explicitly resolves size dependence, while MAM7 represents it implicitly through modal critical supersaturation (Abdul-Razzak and Ghan, 2000).

https://doi.org/10.5194/egusphere-2026-6624
Preprint. Discussion started: 10 November 2026
© Author(s) 2026. CC BY 4.0 License.

7) ***Cloud droplet nucleation:*** PAMT uses a Quasi-steady-state approximation of the cloud Droplet Growth Equation (QDGE) scheme to represent cloud droplet activation (Wang et al., 2022b). This scheme assumes that supersaturation remains quasi-steady within the subgrid-scale layer, enabling efficient simulation of aerosol activation, the vertical supersaturation profile, and the initial droplet number concentration near the cloud base. It can be regarded as a simplified parcel model suitable for use in climate models. MAM7 uses a physically-based parameterization proposed by Abdul-Razzak and Ghan (2000).

8) ***Ice nucleation:*** PAMT and MAM7 largely retains the default ice nucleation scheme in CIESM, which treats homogeneous and heterogeneous freezing of SO4 and DU in mixed-phase and cirrus clouds and estimates subgrid vertical velocity using the turbulent kinetic energy (Liu et al., 2007). Due to large uncertainties, BC is not considered as an ice nucleus by default (Gettelman et al., 2012).

9) ***Dry deposition:*** Both PAMT and MAM7 calculate aerosol dry deposition using the resistance-based parameterization of Zhang et al. (2001) , in which the dry deposition velocity is determined by gravitational settling and aerodynamic and surface resistances. However, PAMT adopts the revised scheme of Emerson et al. (2020), which incorporates observational constraints, whereas MAM7 uses the original framework. In addition, MAM7 distinguishes interstitial and cloud-borne aerosols based on wet particle and droplet sizes, respectively, while PAMT applies a tunable Stokes-number-dependent sticking parameter to represent particle attachment efficiency for different aerosol species and surface types (Emerson et al., 2020; Zhang et al., 2001).

10) ***Wet deposition:*** In PAMT, wet deposition includes rainout, washout, and resuspension for both stratiform and convective clouds. Rainout removes activated (cloud-borne) aerosols during cloud-to-precipitation conversion, while washout scavenges interstitial aerosols by rain and snow using size-dependent collection efficiencies (Croft et al., 2009; Scott, 1978). Aerosols are resuspended in proportion to the fraction of precipitation that evaporates or sublimates. MAM7 adopts a similar framework, with wet removal rates linked to cloud microphysics, aerosol solubility, and precipitation (Barth et al., 2000; Easter et al., 2004; Rasch et al., 2000).

2.1.3 Aerosol Optical Properties

To enable interactive aerosol–radiation coupling, PAMT calculates aerosol optical properties, including extinction coefficient, single-scattering albedo, and asymmetry factor, and passes them to the radiation module to compute aerosol radiative effects (Iacono et al., 2008; Mlawer et al., 1997). Because the original CIESM interface was developed for MAM3/MAM7, new offline lookup tables were generated for each longwave and shortwave spectral band based on the aerosol mixing states represented in PAMT. Five aerosol species (SO4, BC, OA, DU, and SS) are considered. Hygroscopic growth is represented using the κ-Köhler framework (Petters and Kreidenweis, 2007), while aerosol optical properties are taken from Li et al. (2001, 2008) for SO4 and SS, Peng et al. (2012) for DU, d'Almeida (1991) for BC, and Peters et al. (2010) for OA. A key feature is the explicit treatment of internal mixing among SO4, BC, and OA, with optical properties parameterized in a six-dimensional lookup table describing particle size, relative humidity, and chemical composition. This representation accounts for absorption

https://doi.org/10.5194/egusphere-2026-6624
Preprint. Discussion started: 10 November 2026
© Author(s) 2026. CC BY 4.0 License.

enhancement caused by internal mixing and provides a physically consistent treatment of aerosol–radiation interactions. In addition, diagnosed cloud condensation nuclei (CCN) and ice nuclei (IN) concentrations are coupled to the cloud microphysics schemes to represent aerosol–cloud interactions, enabling fully interactive aerosol–radiation–cloud coupling.

2.1.4 Others

All aerosol modules coupled within CIESM use a two-moment approach, predicting both the number concentration and mass mixing ratio for different aerosol species. Variables that need to be transported across the model grid with the three-dimensional wind field are referred to as tracers. In CIESM-MAM7, there are 31 aerosol-related tracers, including 7 number concentration tracers (one per mode) and 24 mass concentration tracers (one per component in each mode). In CIESM-PAMT, there are 24 aerosol-related tracers, comprising 9 number concentration tracers (3 internal mixtures, 6 external mixtures) and 15 mass concentration tracers (9 internal, 6 external). Since more tracers require more inter-grid transport, increasing computational cost, CIESM-PAMT is theoretically more efficient than CIESM-MAM7 in terms of tracer count.

By integrating the PAMT module into CIESM, nearly all aerosol processes have been updated. CIESM-PAMT retains the advantages of the original model while providing a more detailed representation of aerosol size distributions, mixing states, source–sink processes, and coupling with cloud microphysics. This enhances the model's capability to evaluate aerosol–cloud–climate interactions.

2.2 Cloud Microphysics in CIESM

The microphysics scheme of the stratiform cloud used in CIESM is a two-moment scheme (MG1.5) (Morrison and Gettelman, 2008), which prognoses both number concentrations and mass mixing ratios of cloud/ice/rain/snow in large-scale clouds. The represented processes include activation of CCN and deposition/condensation-freezing nucleation on IN to form cloud droplets and ice crystals; condensation/deposition, evaporation/sublimation, autoconversion of cloud droplets and cloud ice to rain and snow, accretion of cloud droplets and ice by precipitation, heterogeneous and homogeneous freezing, melting, sedimentation, convective detrainment, and ice multiplication through the rime-splintering process (Morrison and Gettelman, 2008).

CIESM further improves ice cloud calculations by developing an enhanced ice microphysics scheme based on MG1.5, referred to as the single-ice scheme (Zhao et al., 2017). This scheme represents the riming growth of ice particles through a diagnosed riming intensity and treats ice crystals and snow as a single prognostic variable, which improves computational efficiency and reduces uncertainties associated with ice–snow conversion parameterizations, thereby avoiding explicit parameterizations of ice–snow conversion, reducing related uncertainties, improving computational efficiency, and enhancing the simulation of high clouds and longwave radiation (Zhao et al., 2017). In contrast to NCAR CESM1.2.1, CIESM also incorporates microphysical processes into its convection parameterization (Song and Zhang, 2011), which substantially improves the simulation of the vertical structure and radiative properties of convective clouds (Song and Zhang, 2011; Storer et al., 2015).

Based on this framework, we replaced the default COSP1.3 (the Cloud Feedback Model Intercomparison Project Observational Simulator Package, version 1.3) (Bodas-Salcedo et al., 2011) in CIESM with the COSP1.4 implementation of Guo et al. (2020),

https://doi.org/10.5194/egusphere-2026-6624
Preprint. Discussion started: 10 November 2026
© Author(s) 2026. CC BY 4.0 License.

following the framework described by Kay et al. (2016). This upgrade enables direct comparisons between model-simulated and satellite-observed cloud properties. In addition, we also accounted for the influence of pre-existing ice crystals on homogeneous ice nucleation (Shi et al., 2015), and adjusted the minimum cloud droplet number concentration in in-cloud grid cells from 0 to 30 cm^{-3} based on observations (Jia and Quaas, 2023), in line with the range of 20–40 cm^{-3} used by Neubauer et al. (2019).

2.3 Radiative Transfer in CIESM

The longwave and shortwave radiative transfer calculations in CIESM are performed using the Rapid Radiative Transfer Model for General circulation models (RRTMG) (Iacono et al., 2008; Mlawer et al., 1997). For radiative calculations involving clouds and aerosols, the model first reads precomputed optical property look-up tables and then performs the radiative transfer calculations based on the diagnosed cloud and aerosol properties. For aerosol–radiation interactions, RRTMG requires spectrally resolved aerosol optical properties, including extinction coefficient, single-scattering albedo, and asymmetry factor (Iacono et al., 2008). Although MAM7 and PAMT use different aerosol representations, both provide these quantities to RRTMG. In PAMT, they are diagnosed from aerosol size distributions, hygroscopic growth, and mixing states using offline lookup tables, as described in Section 2.1.3, ensuring a consistent interface with the radiation scheme. For aerosol–cloud interactions, radiative calculations for warm clouds rely on cloud optical properties, including the cloud droplet mass and number mixing ratios and droplet size parameters, such as the effective radius (R_e) or the gamma distribution shape (μ) and slope (λ) parameters. For ice-phase clouds, the corresponding inputs are the ice particle mass and number mixing ratios and the ice crystal effective diameter (D_i).

2.4 Separation of Aerosol–cloud Interactions

In general circulation models (GCMs), the total effective radiative forcing of ACI (F_{aci}) is typically estimated from differences in net radiative fluxes between two sets of emission experiments. One experiment uses pre-industrial (PI) aerosol emissions, commonly represented by the year 1850, while the other uses present-day (PD) aerosol emissions, sometimes represented by the year 2010 (Jia et al., 2021; Myhre et al., 2017). Both the PI and PD emission inventories follow the CMIP6 specifications (Hoesly et al., 2018). To minimize the influence of other factors, the two experiments are conducted with identical sea surface temperatures, sea ice fields, and greenhouse gas concentrations. The difference in net radiative flux at the top of the atmosphere (TOA) between the two experiments represents the total aerosol effective radiative forcing (ERF) (Ghan, 2013; Gryspeerdt et al., 2020; Myhre et al., 2013). The ERF can be decomposed into contributions from ARI, ACI, and surface albedo effects. In models, ARI usually is diagnosed from the difference between all-sky and clear-sky TOA fluxes, while the residual is attributed to ACI and surface albedo contributions. Note that in this study, surface albedo changes are negligible due to prescribed land surface conditions, and thus are not explicitly separated in the diagnostic framework. However, von Salzen et al. (2022) found that black carbon-induced snow albedo forcing substantially contributes to near-term radiative forcing changes in the Arctic.

https://doi.org/10.5194/egusphere-2026-6624
Preprint. Discussion started: 10 November 2026
© Author(s) 2026. CC BY 4.0 License.

This effect is not considered here but could be included in future work to better assess aerosol radiative effects over snow-covered regions.

Like most GCMs, CIESM can only calculate the total effective ACI radiative forcing, and does not inherently separate the radiative contributions from individual ACI processes. However, satellite-based estimates of ACI radiative forcing largely reflect the radiative forcing associated with the Twomey effect (Twomey, 1977), which leads to a mismatch between satellite-derived and model-simulated estimates (Bellouin et al., 2020; Jia et al., 2021; Quaas et al., 2008). The Partial Radiative Perturbation (PRP) method proposed by Mülmenstädt et al. (2019) enables the separation of radiative contributions from different aerosol effects within models, making it possible to investigate the impacts of individual processes on ACI. In this study, we implement this method by adding diagnostic code to the RRTMG to quantify radiative forcing associated with different ACI effects. For liquid clouds, these include radiative forcing due to the Twomey effect (F_{N_d}), as well as rapid adjustments in liquid water path and cloud fraction (F_{q_l} and F_{f_l}). When the influence of aerosols on ice-cloud optical properties is considered, the PRP method can also separate effects in mixed-phase and ice clouds, including radiative forcing due to increases in ice-nucleating particles (F_{N_i}) and adjustments in ice water path and cloud fraction (F_{q_i} and F_{f_i}). A detailed description of the PRP method and its implementation in CIESM is provided in the Appendix A.

2.5 Model Configuration and Experimental Design

In this study, both the PAMT and MAM7 modules were implemented in CIESM and run in parallel to enable a direct comparison of their simulated results. To minimize the influence of internal climate variability and differences in external forcing, all simulations were driven by the same observed, time-varying sea surface temperature and sea ice fields (Eyring et al., 2016), as well as CMIP6 historical emissions of aerosols and their precursor gases (Hoesly et al., 2018). In addition, horizontal winds were constrained toward the ECMWF fifth-generation reanalysis (ERA5) using a Newtonian relaxation (nudging) technique (Hersbach et al., 2020; Kooperman et al., 2012; Wang et al., 2020), ensuring that differences between simulations primarily originated from the aerosol modules.

The model was run at a horizontal resolution of f19_g16, corresponding to a finite-volume grid of 1.9° × 2.5° for the atmosphere and land components and a dipole grid of 1.125° × 0.27–0.54° for the ocean and sea ice components. The vertical discretization consisted of 30 hybrid sigma-pressure levels, with a model time step of 30 minutes. For the evaluation of clouds, precipitation, and radiation, the model was integrated for 15 years (2000–2014), and the corresponding observational datasets were used for model assessment.

To investigate ACI, pairs of simulations were conducted using two different emission scenarios: PI and PD conditions. The year 1850 was adopted to represent PI emissions and 2010 to represent PD emissions (Jia et al., 2021; Myhre et al., 2017). To isolate aerosol effects and reduce the influence of other factors, both sets of simulations were performed with identical 2010 sea surface temperatures, sea ice fields, and greenhouse gas concentrations. Following the protocol of the PRP method, the model was integrated for 6 years under both PI and PD conditions, and the final 5 years were used for analysis. It should be

https://doi.org/10.5194/egusphere-2026-6624
Preprint. Discussion started: 10 November 2026
© Author(s) 2026. CC BY 4.0 License.

noted that, in the ACI experiments, cloud microphysical processes within the deep convection scheme were switched off. This choice was motivated by two considerations. First, aerosol–cloud interactions in deep convective clouds are estimated to make only a relatively small contribution to the global aerosol effective radiative forcing (approximately −0.08 W m^{-2}, Langton et al. (2021)). Second, aerosol effects in deep convection remain highly uncertain because of the substantial uncertainties associated with deep convective parameterizations in current global climate models (Lin et al., 2022). Consequently, the diagnosed ACI effective radiative forcing in this study originates exclusively from large-scale stratiform cloud processes. This approach is consistent with common practice in previous studies aimed at isolating aerosol–cloud interaction effects in large-scale clouds (Bellouin et al., 2020; Jia et al., 2021; Quaas et al., 2008).

Uncertainty associated with choices of tuning factors is a critical issue in climate model development and should be documented in a transparent and traceable manner (Hourdin et al., 2017). Accordingly, a clear strategy for setting tunable parameters was defined prior to the simulations. The overarching goal was to minimize parameter tuning while sequentially satisfying the following priorities: (i) achieving near-closure of the TOA shortwave and longwave radiation budget; (ii) ensuring good agreement between simulated and observed cloud radiative effects; and (iii) improving the consistency of cloud fraction, cloud water path, and precipitation with observations. All tunable parameters were constrained to physically reasonable ranges. During the tuning process, TOA radiative balance was prioritized, followed by progressive optimization of other fields. Parameter tuning was applied primarily to the CIESM-MAM7 due to it is the original configuration. The tuning strategy, the physical meanings of the tunable parameters, and their final recommended values are described in detail in Part 1. To ensure a direct and consistent comparison between the two aerosol modules, CIESM-PAMT adopted the same parameter settings as CIESM-MAM7, thereby maintaining an identical model configuration apart from the aerosol representation.

3 Data

3.1 Cloud Condensation Nuclei

$CCN02$ refers to the cloud condensation nuclei (CCN) number concentration at a supersaturation of 0.2%. CCN concentration is a key quantity for studies of cloud droplet formation because it represents the potential of aerosol particles to activate into cloud droplets at a specified supersaturation. Therefore, agreement with observed CCN concentrations provides an important evaluation of the simulated aerosol number concentration, size distribution, and hygroscopic properties, although it does not by itself guarantee accurate aerosol activation or cloud droplet number predictions. Therefore, $CCN02$ is widely used in model evaluations of aerosol/droplet number concentrations (Fanourgakis et al., 2019; Pierce and Adams, 2009; Schmale et al., 2017; Schmidt et al., 2012; Wang et al., 2022a). Fanourgakis et al. (2019) evaluated the performance of 14 global climate and chemistry models in simulating near-surface $CCN02$ concentrations using ground-based observations. They found that the models generally underestimated $CCN02$ concentrations in the lowest model level by about 36%, highlighting the need for improved representation of aerosol processes.

https://doi.org/10.5194/egusphere-2026-6624
Preprint. Discussion started: 10 November 2026
© Author(s) 2026. CC BY 4.0 License.

In this study, we use the same ground-based dataset (CCN02_SITE) employed in Fanourgakis et al. (2019) to evaluate near-surface $CCN02$ simulated by CIESM. This dataset includes eight European sites (Cabauw, Finokalia, Jungfraujoch, Mace Head, Melpitz, Puy de Dôme, Hyytiala, and Vavihill) and one Japanese site (Noto Peninsula) (Schmale et al., 2017). Additionally, we supplement the dataset with two Chinese sites (Xinzhou and Xianghe) to assess CCN conditions in regions with strong anthropogenic aerosol influence (Zhang et al., 2022).

While ground-based $CCN02$ measurements are accurate, they lack global coverage. To evaluate CIESM's global performance in simulating $CCN02$, we also use a satellite-derived data (CCN_SAT) developed by Choudhury and Tesche (2023). CCN_SAT was derived from the Cloud-Aerosol Lidar and Infrared Pathfinder Satellite Observations (CALIPSO) retrievals using the recently introduced Optical Modelling of the CALIPSO Aerosol Microphysics (OMCAM) algorithm (Choudhury and Tesche, 2022). While this dataset provides valuable global coverage of CCN profiles, it also has several known limitations. Due to the CALIOP aerosol detection threshold, aerosol layers with very low extinction, particularly in the clean free troposphere, may not be detected, resulting in incomplete sampling. In addition, CCN retrievals near the surface are subject to larger uncertainties because strong backscatter from sea-salt aerosols can lead to an overestimation of CCN concentrations over oceans. Comparison with ground-based observations indicates that CCN_SAT tends to overestimate $CCN02$, with a global-scale overestimation of roughly 22% (Choudhury and Tesche, 2022). Following the recommendation of the dataset developers (Choudhury, personal communication), only retrievals above 500 m are used in this study to reduce these biases. Overall, the satellite-derived CCN dataset is used as a complementary dataset for large-scale evaluation, while ground-based observations provide the primary benchmark for model assessment.

To place CIESM's performance in context and guide model improvements, we also include the multi-model results evaluated in Fanourgakis et al. (2019) (denoted CCN02_MOD) for comparison in the $CCN02$ assessment.

3.2 Clouds

Global-scale evaluations of cloud properties mainly rely on satellite retrievals. The satellite products used in this study include the Moderate Resolution Imaging Spectroradiometer (MODIS) (Platnick et al., 2003), CALIPSO (Winker et al., 2009), CloudSat (Stephens et al., 2002), Advanced Along-Track Scanning Radiometer (AATSR) (Bevan et al., 2012), Advanced Very High Resolution Radiometer (AVHRR) (Holben, 1986), Visible Infrared Imaging Radiometer Suite (VIIRS) (Justice et al., 2013), Polarization and Directionality of the Earth's Reflectances (POLDER) (Deschamps et al., 1994), and International Satellite Cloud Climatology Project (ISCCP) (Rossow and Schiffer, 1991). Satellites do not observe cloud variables directly. Instead, they measure radiances in specific spectral bands and viewing geometries, and then derive cloud properties using mathematical–physical retrieval algorithms. Below, we introduce the main retrieval algorithms and datasets based on these satellite missions.

Cloud variables in GCMs are obtained in a fundamentally different way from satellite retrievals. Models calculate them directly from parameterizations and grid-resolved variables, rather than inferring them from observed radiances. As a result, model-simulated and satellite-retrieved variables may share the same names but represent different physical quantities. To address

https://doi.org/10.5194/egusphere-2026-6624
Preprint. Discussion started: 10 November 2026
© Author(s) 2026. CC BY 4.0 License.

this inconsistency, the CFMIP Observation Simulator Package (COSP) was developed. COSP mimics the satellite retrieval process within GCMs, making model outputs more directly comparable to satellite products (Bodas-Salcedo et al., 2011). To further facilitate model–observation comparisons, several satellite products have been specifically tailored for model evaluation, such as the MODIS-based MCD06COSP (Pincus et al., 2023) and the CALIPSO-based CALIPSO-GOCCP (Chepfer et al., 2010). MCD06COSP integrates cloud property observations from MODIS Terra and Aqua and is more suitable for comparison with model simulations. Available variables include total/high/middle/low/liquid/ice cloud fractions, liquid/ice water paths, cloud droplet effective radius, and so on. However, the COSP version used in the current CIESM (COSP1.4) contains known bugs in simulating cloud fraction by altitude for MODIS-type diagnostics (Hubanks et al., 2023). Therefore, high/middle/low cloud fractions from MCD06COSP are not used for evaluation in this study. As a complement, cloud fraction evaluation is also based on the CALIPSO simulator in COSP1.4 and the corresponding CALIPSO-GOCCP dataset, which is widely used for evaluating total/high/middle/low cloud fractions (Chepfer et al., 2010).

In addition, several algorithms and datasets have been developed to retrieve cloud droplet number concentration (N_d), cloud droplet effective radius (R_e), liquid water path (LWP), and ice water path (IWP) from satellite observations. A brief overview is provided below.

Building on earlier work, Quaas et al. (2006) proposed a method to derive cloud-top N_d for liquid clouds using MODIS cloud optical thickness and effective radius (hereafter Quaas06). This approach has since been extended to produce several widely used N_d datasets, including Bennartz17 (Bennartz and Rausch, 2017), Zhu18 (Zhu et al., 2018), and Grosvenor18 (Grosvenor et al., 2018). These datasets apply different sampling strategies to the underlying MODIS observations (Gryspeerdt et al., 2022), which are used here to evaluate the model performance in simulating cloud-top N_d.

Multiple satellite datasets are currently available for retrieving cloud droplet effective radius (R_e), but systematic differences exist among sensors and retrieval algorithms. Previous studies have shown that satellite-derived R_e is generally biased high relative to airborne in situ observations, likely due to factors such as cloud vertical structure, viewing geometry, optical thickness thresholds, and underlying algorithmic assumptions (King et al., 2013; Di Noia et al., 2019; Shang et al., 2019; Zhang and Platnick, 2011). To assess the consistency and uncertainty of R_e retrievals, this study employs multiple satellite products (Re-Multi), including MODIS, VIIRS, AVHRR, and POLDER, to conduct a comparative analysis of the agreement and discrepancies among different observing platforms in retrieving cloud microphysical properties.

In GCMs, the simulated liquid and ice water paths (LWP and IWP) generally refer to non-precipitating cloud condensate, i.e., suspended cloud droplets and ice crystals, excluding precipitating hydrometeors such as rain, graupel, and snow. In contrast, satellite-retrieved liquid and ice water paths usually represent total water paths, because the observing instruments do not actively filter out precipitating particles, making these products not directly comparable with model outputs. Elsaesser et al. (2017) combined observations from eight satellites to produce the MAC-LWP dataset, which excludes precipitating particles and is therefore suitable for direct evaluation of climate model simulations. Delanoë and Hogan (2008) merged CALIPSO, CloudSat, and MODIS observations to develop the DARDAR dataset, which has been widely used in ice cloud studies. For example, Li et al. (2012) used DARDAR to construct an IWP product that excludes precipitating ice particles (IWP_Li),

https://doi.org/10.5194/egusphere-2026-6624
Preprint. Discussion started: 10 November 2026
© Author(s) 2026. CC BY 4.0 License.

allowing a more accurate evaluation of model-simulated IWP. In addition, Doktorowski et al. (2024) produced a similar dataset (IWP_LIM) following this methodology. These two datasets are used in this study to evaluate the performance of CIESM in simulating IWP.

In summary, this study uses multiple satellite products to evaluate cloud properties in CIESM. The MCD06COSP dataset provides total cloud fraction (CLT), liquid cloud fraction (CLW), and ice cloud fraction (CLI), while CALIPSO-GOCCP provides CLT as well as high-, mid-, and low-level cloud fractions (CLH, CLM, and CLL). The Quaas06, Bennartz17, Zhu18, and Grosvenor18 datasets provide cloud droplet number concentration (N_d). Cloud droplet effective radius (R_e) is derived from MODIS, VIIRS, AVHRR, and POLDER, MAC-LWP provides liquid water path (LWP), and IWP_Li and IWP_LIM provide ice water path (IWP).

3.3 Precipitation and Radiation

Aerosol effects on cloud microphysical properties ultimately modify cloud lifetime and radiative characteristics. Therefore, this study also evaluates the performance of CIESM in simulating precipitation and radiative fluxes.

Two observational precipitation datasets are used for model evaluation: the Global Precipitation Climatology Project (GPCP) (Huffman et al., 1997, 2009) and the Tropical Rainfall Measuring Mission (TRMM) (Huffman et al., 2007). GPCP is a global gridded precipitation dataset produced under the World Climate Research Programme. It combines rain gauge observations and satellite retrievals and provides monthly products at 1° × 1° resolution for the period since 1979. TRMM provides precipitation products over the tropics and subtropics (47°S-47°N or so) based on satellite observations. Compared with GPCP, TRMM has higher spatial resolution (0.25° × 0.25°), but more limited spatial coverage and a shorter temporal record (from 1998 to the present). These two datasets are jointly used to evaluate CIESM's simulation for precipitation rate ($Prec$).

Radiative fluxes at the top of the atmosphere (TOA) are evaluated using the CERES Energy Balanced and Filled Top-of-Atmosphere (EBAF-TOA) Edition 4.1 monthly dataset, which combines CERES observations from the Terra and Aqua satellites to provide globally consistent, energy-balanced TOA radiative fluxes (Kato et al., 2013; Loeb et al., 2018). The CERES instruments, flying on the Terra and Aqua satellites, observe radiation in shortwave (0.3–5.0 μm), longwave (8–12 μm), and broadband (0.3 to >100 μm) channels, and provide both all-sky and clear-sky radiative flux products at TOA and within cloud layers. CERES is used to assess CIESM-simulated shortwave, longwave, and net radiative fluxes at TOA under all-sky conditions (SW, LW, and Net), as well as the shortwave, longwave, and net cloud radiative effects (SW_CRE, LW_CRE, and Net_CRE).

To match the simulation period of CIESM, precipitation and radiation datasets for 2000–2014 are used in this study.

3.4 Aerosol–cloud Interactions

This study also compares the simulated ACI with observation-based estimates. However, current observational constraints on ACI radiative forcing remain poorly characterized for effects other than the Twomey effect–induced forcing (F_{Nd}), and the

https://doi.org/10.5194/egusphere-2026-6624
Preprint. Discussion started: 10 November 2026
© Author(s) 2026. CC BY 4.0 License.

associated estimates are subject to substantial uncertainty (IPCC, 2023). Therefore, this study focuses on a detailed evaluation of the global distribution of F_{Nd}, while the global mean total ACI radiative forcing is taken from the observation-based estimate reported in the IPCC AR6, namely -1.0 ± 0.7 W m^{-2} (medium confidence).

Satellite-based ACI radiative forcing typically exclude grids without co-located aerosol observations, introducing substantial sampling bias and leading to a systematic underestimation of F_{Nd} (Jia et al., 2021). By combining MODIS with reanalysis data, Jia et al. (2021) reduced this bias and developed a new global, sampling-bias-corrected F_{Nd} dataset (denoted as Jia2021), which provides an important benchmark for model evaluation. This dataset has a horizontal resolution of 1° × 1° and covers the region between 60°S and 60°N, and is used to evaluate the performance of CIESM in representing Twomey effect.

3.5 Summary of Datasets

This study compiles an integrated, multi-source, multi-variable, and multi-scale observational framework that spans key processes from cloud condensation nuclei to clouds, precipitation, radiation, and aerosol–cloud interactions. This dataset provides a comprehensive basis for evaluating the performance of CIESM, identifying its strengths and limitations, and guiding subsequent model development. An overview of the datasets used in this study is given in Table 1.

Table 1. Overview of datasets used for CIESM evaluation in this study. Abbreviations are defined in the main text.

Variable	Dataset	Data source	Variable	Time period	Reference
CCN	CCN_SITE	Ground stations	$CCN02$	2011 - 2014	(Schmale et al., 2017; Zhang et al., 2022)
	CCN_SAT	CALIPSO		2006 - 2014	(Choudhury and Tesche, 2022)
	CCN_MOD	Multi-models		2011	(Fanourgakis et al., 2019)
Cloud	MCD06COSP	MODIS	CLT, CLW, and CLI	2003 - 2014	(Pincus et al., 2023)
	CALIPSO-GOCCP	CALIPSO	CLT, CLH, CLM, and CLL	2007 - 2014	(Chepfer et al., 2010)
	ISCCP	ISCCP	CLT	2000 - 2014	(Rossow and Schiffer, 1991)
	Quaas06, Bennartz17, Zhu18, Grosvenor18	MODIS	N_d	2003 - 2014	(Gryspeerdt et al., 2022)
	Re-Multi	MODIS, AVHRR, VIIRS, POLDER	R_e	2000 - 2014	(Justice et al., 2013; Nakajima and King, 1990; Pincus et al., 2023; Shang et al., 2019)
	MAC-LWP	multi-satellites	LWP	2000 - 2014	(Elsaesser et al., 2017)
	IWP_Li, IWP_LIM	CALISPO, CloudSat, and MODIS	IWP	2007 - 2009	(Doktorowski et al., 2024; Li et al., 2012)
Precipitation	GPCP	Multi-satellites and ground stations	$Prec$	2000 - 2014	(Huffman et al., 1997, 2009)
	TRMM	TRMM	$Prec$	2000 - 2014	(Huffman et al., 2007)
Radiation	CERES	CERES	SW, LW, Net, SW_CRE, LW_CRE, and Net_CRE	2000 - 2014	(Kato et al., 2013; Loeb et al., 2018)
ACI	Jia2021	MODIS, MERRA-2	F_{Nd}	/	(Jia et al., 2021)

https://doi.org/10.5194/egusphere-2026-6624
Preprint. Discussion started: 10 November 2026
© Author(s) 2026. CC BY 4.0 License.

4 Results

4.1 Evaluation of Cloud Condensation Nuclei

In this study, $CCN02$ is used to evaluate CIESM, with a focus on how differences in aerosol size distributions, mixing states, and hygroscopicity between PAMT and MAM7 affect the simulation of aerosol activation. Using $CCN02$ minimizes the influence of environmental variability and enables a more robust assessment of the activation schemes.

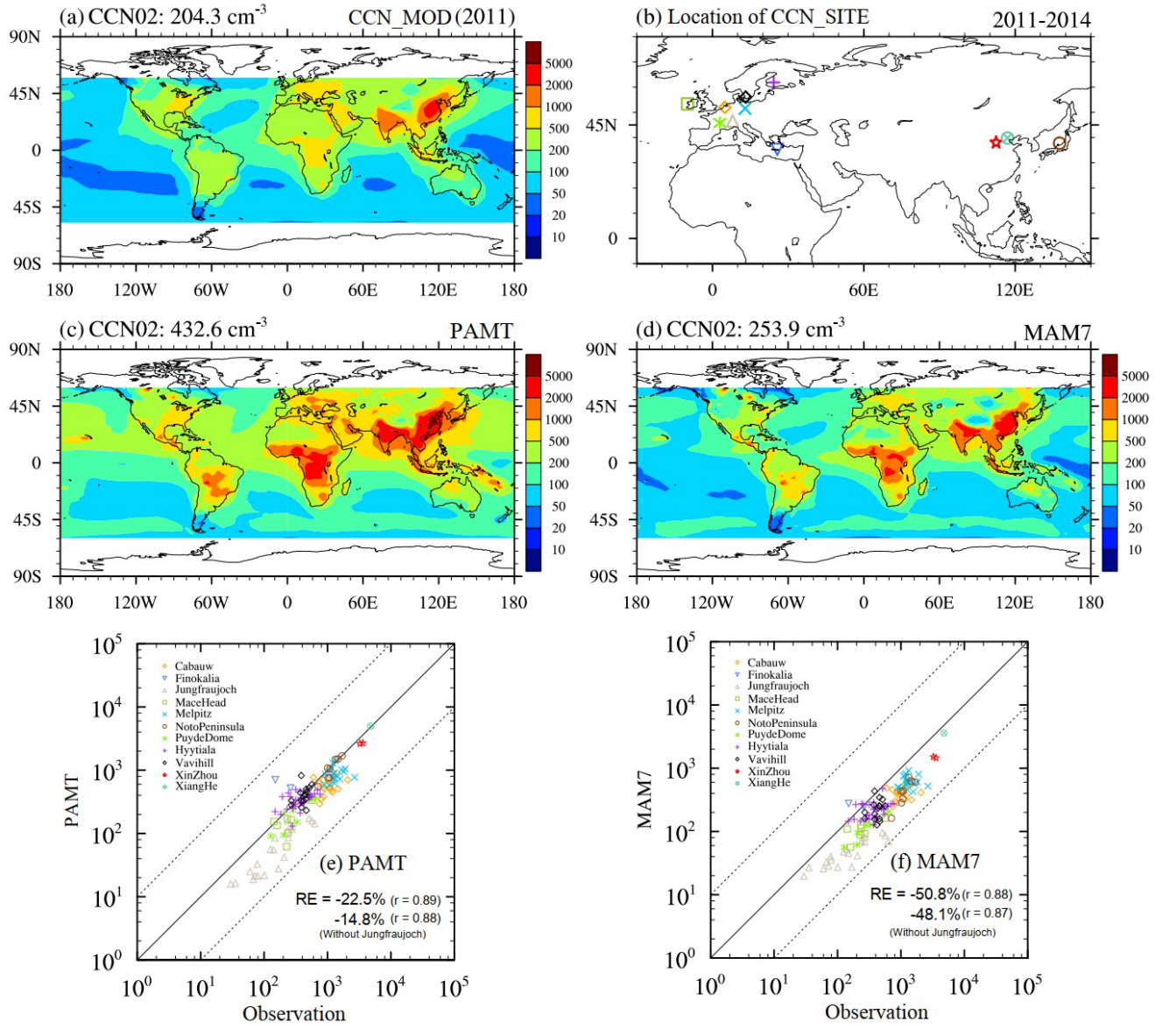


Figure 2. Spatial distribution and scatter comparison of cloud condensation nuclei number concentration at 0.2% supersaturation ($CCN02$) from CIESM-PAMT/MAM7, the multi-model mean (CCN_MOD), and site observations (CCN_SITE) (unit: cm⁻³). The relative error (RE) and Pearson correlation coefficient (r) are reported in the bottom-right corner of panels (e-f).

https://doi.org/10.5194/egusphere-2026-6624
Preprint. Discussion started: 10 November 2026
© Author(s) 2026. CC BY 4.0 License.

Figure 2 shows the $CCN02$ results from the multi-model mean (CCN_MOD), surface-based observations (CCN_SITE), and simulations from CIESM-PAMT and CIESM-MAM7. Here the CIESM outputs were interpolated to observation sites using linear interpolation in the vertical and bilinear interpolation in the horizontal. Compared with the multi-model mean (Fig. 2a), CIESM simulates higher global-mean $CCN02$, particularly over continental regions (Figs. 2c, d). Relative to site observations, both aerosol modules underestimate $CCN02$ despite their high bias relative to the multi-model mean, with biases of −22.5% and −50.8% for CIESM-PAMT and CIESM-MAM7, respectively, indicating better performance by CIESM-PAMT. In addition, CIESM-PAMT shows a slight improvement in correlation with the observations, although the improvement is not statistically significant (Fig. 2e-f). A more detailed analysis shows that the apparent underestimation at surface sites is largely influenced by high-altitude stations such as Jungfraujoch (3580 m a.s.l., Swiss Alps). It should be noted that such mountain sites are not fully representative of the coarse-resolution model grid cells, as the model does not explicitly resolve complex topography and associated mountain–valley circulation systems. Consequently, simulated near-surface CCN concentrations at these locations tend to reflect free-tropospheric background conditions, which can lead to a systematic low bias relative to observations influenced by local boundary-layer processes. Excluding this site reduces the relative biases to −14.8% for CIESM-PAMT and −48.1% for CIESM-MAM7, although both modules still exhibit underestimation. Overall, the near-surface $CCN02$ simulated by CIESM-PAMT and CIESM-MAM7 is comparable to the multi-model ensemble but exhibits a general low bias, while showing better agreement with the more accurate in situ observations. Among the two schemes, CIESM-PAMT performs better than CIESM-MAM7, with smaller relative deviations from the surface measurements.

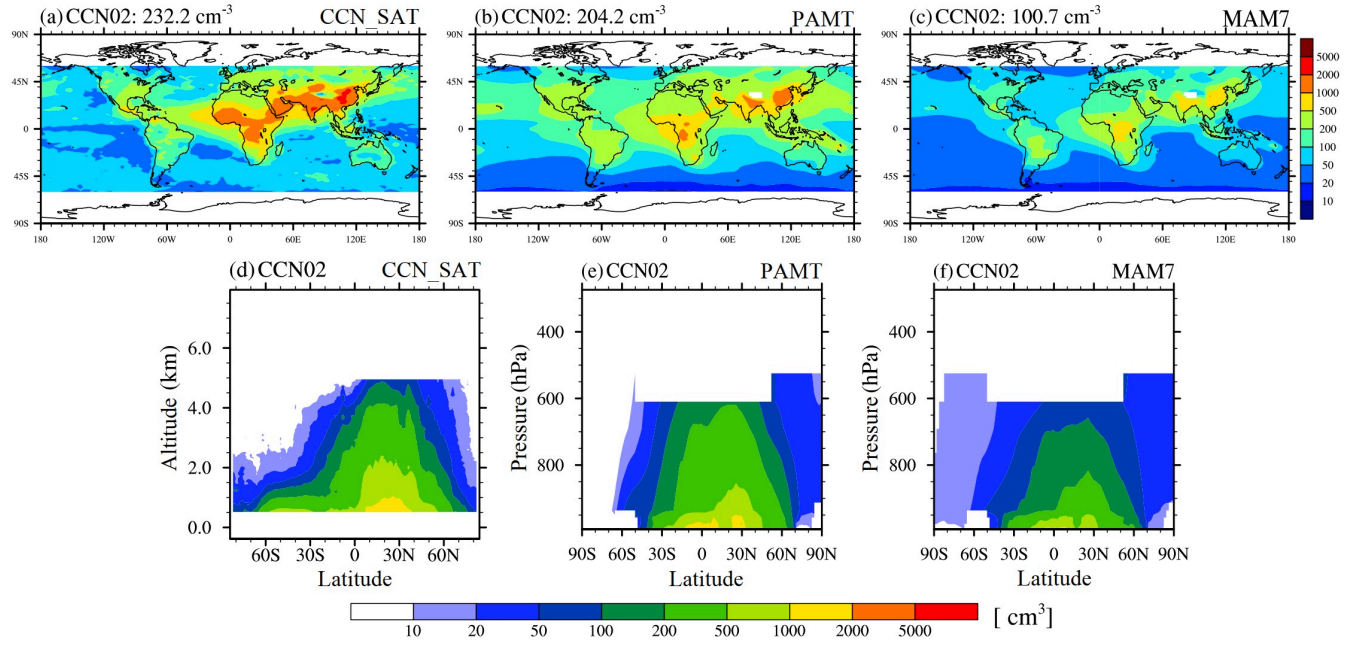


Figure 3. Comparison of cloud condensation nuclei concentration at 0.2% supersaturation ($CCN02$) simulated by CIESM-PAMT/MAM7 with satellite-derived vertically averaged values (500–5000 m, weighted by altitude) and vertical profiles. Note that the vertical coordinates differ between CALIPSO and the model outputs. Unit: cm^{-3}.

https://doi.org/10.5194/egusphere-2026-6624
Preprint. Discussion started: 10 November 2026
© Author(s) 2026. CC BY 4.0 License.

The above evaluation is limited to near-surface observations, as in situ vertical measurements of $CCN02$ are sparsely distributed worldwide. To address the lack of vertical $CCN02$ observations, Choudhury and Tesche (2023) derived the global vertical distribution of $CCN02$ from CALIPSO satellite data. Their results indicate that the retrievals agree well with independent observations above the near-surface layer with height > 500 m, although the product exhibits an overall high bias of about 22% (Choudhury and Tesche, 2023). Figure 3 shows the spatial distribution of vertically averaged (500–5000 m) CCN02 from satellite observations and model simulations, as well as their vertical profiles. In terms of spatial patterns, both PAMT and MAM7 underestimate $CCN02$ relative to the satellite product, with global mean biases of −12% and −57%, respectively. Considering that the CALIPSO-based product itself is positively biased (with an expected global mean of about 200 cm^{-3}), the CIESM-PAMT simulation shows closer agreement with observations. In the vertical dimension, CIESM-PAMT also better reproduces the CALIPSO-derived $CCN02$ profiles, particularly at higher altitudes (Fig. 3e). Overall, these results demonstrate that coupling PAMT substantially improves the simulation of aerosol activation in CIESM, with improvements evident both near the surface and aloft, as reflected in the better agreement between simulated and observed CCN concentrations. This provides supporting evidence that PAMT better represents the aerosol population relevant to cloud droplet activation, particularly the particles capable of activation at a given supersaturation . Since aerosol activation is the key process linking aerosols and clouds, a more realistic representation of the aerosol population available for activation may improve the model's ability to simulate aerosol–cloud interactions.

4.2 Evaluation of Clouds

Cloud simulation involves the coupled processes of macrophysics, microphysics, and convective cloud schemes. Cloud condensation nuclei (CCN) and ice nuclei (IN) simulated by the aerosol module are passed to both stratiform and convective microphysics, directly influencing the number/concentrations and size distribution of cloud particles. These cloud properties, in turn, affect aerosol source and sink processes through pathways such as wet scavenging, forming a tightly coupled feedback system among multiple model components. In this study, the aerosol module in CIESM has been modified, which inevitably affects cloud simulations. Therefore, this section evaluates simulated cloud properties against global satellite observations, including CALIPSO (CALIPSO-GOCCP), MODIS (MCD06COSP), VIIRS, AVHRR, POLDER, and ISCCP (see Section 3.2). The evaluation focuses on total, high-, mid-, low-, liquid-, and ice-cloud fractions, as well as liquid/ice water paths, cloud droplet number concentration, and cloud droplet effective radius, with the aim of assessing current model performance and identifying pathways for further improvement. For cloud fraction, outputs from the COSP1.4 satellite simulator coupled within CIESM are used to enhance the comparability between model results and satellite retrievals.

Figure 4 compares total cloud fraction (CLT) simulated by CIESM-PAMT and CIESM-MAM7 with various satellite products. The results show that PAMT and MAM7 produce very similar global distributions of CLT, with relative differences in global means below 5%. Both modules underestimate CLT relative to CALIPSO-GOCCP, ISCCP, and MCD06COSP, with global mean relative biases of −10%, −20%, and −23% for PAMT, and −7%, −18%, and −22% for MAM7, respectively. However, the spatial patterns of underestimation differ across satellite datasets. Relative to CALIPSO-GOCCP, the main negative biases

https://doi.org/10.5194/egusphere-2026-6624
Preprint. Discussion started: 10 November 2026
© Author(s) 2026. CC BY 4.0 License.

are concentrated between 30°S and 30°N (Fig. 4d), while comparisons with ISCCP show underestimation across most regions except the Southern Ocean (Fig. 4h). When compared with MCD06COSP, underestimation is evident globally (Fig. 4f). Overall, the simulations of CLT exhibit a systematic underestimation relative to observations and are broadly similar across different aerosol modules.

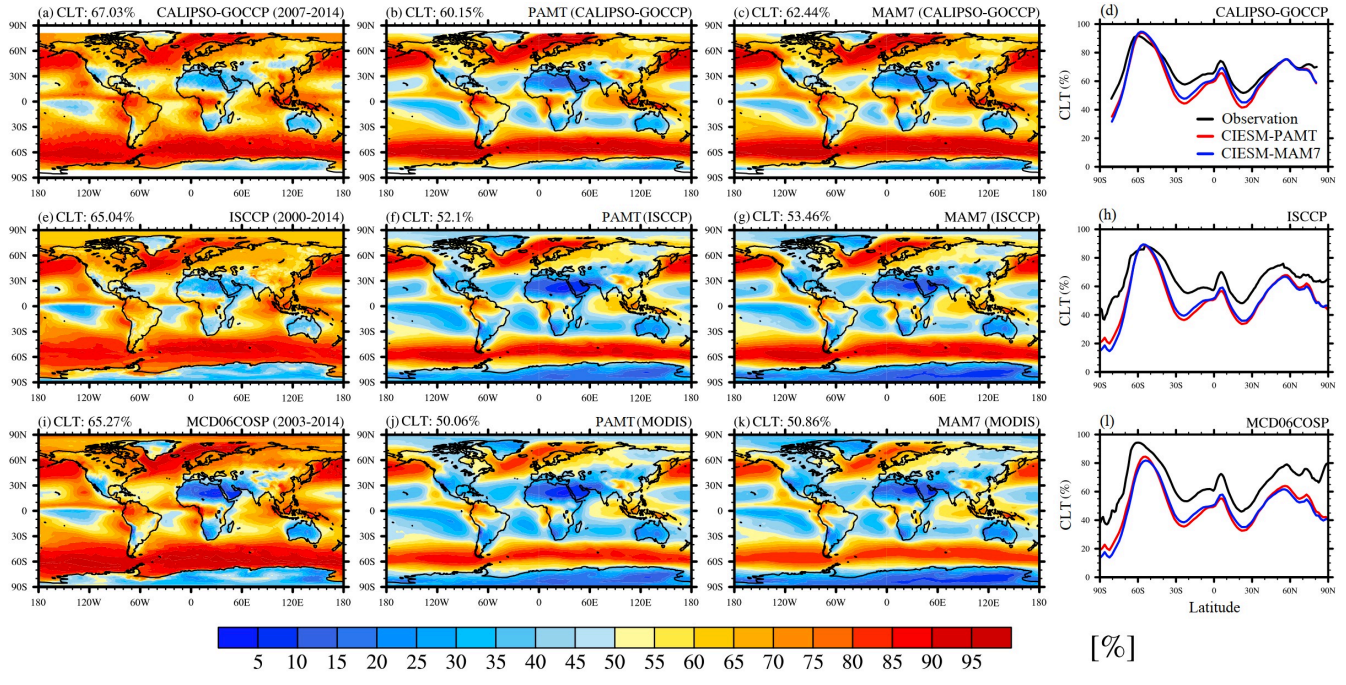


Figure 4. Spatial distribution and zonal-mean comparison of total cloud fraction (CLT) simulated by CIESM-PAMT/MAM7 with CALIPSO-GOCCP, ISCCP, and MCD06COSP. Unit: %.

Figure 5 presents the spatial distribution and zonal mean of clouds at different altitudes (high, middle, and low clouds) as simulated by CIESM-PAMT and CIESM-MAM7, compared with satellite observations. The results indicate that both PAMT and MAM7 produce similar simulations for high clouds (CLH) and low clouds (CLL), with relative deviations below 5%, whereas more pronounced differences are observed in middle clouds (CLM). Specifically, both PAMT and MAM7 underestimate CLH to varying degrees, with relative biases of -11% and -10%, particularly in the mid-latitude regions (Fig. 5d). For CLM, PAMT performs better, showing a slight underestimation of -3%, with zonal mean values nearly coinciding with observations over the Southern Ocean, while MAM7 overestimates CLM by 5% (Fig. 5h). In terms of CLL, both modules underestimate cloud fractions compared with observations (-11% for PAMT and -6% for MAM7), especially along coastal regions such as the eastern Pacific and Atlantic. Overall, the underestimation of total cloud cover by CIESM primarily originates from the biases in high and low cloud simulations.

https://doi.org/10.5194/egusphere-2026-6624
Preprint. Discussion started: 10 November 2026
© Author(s) 2026. CC BY 4.0 License.

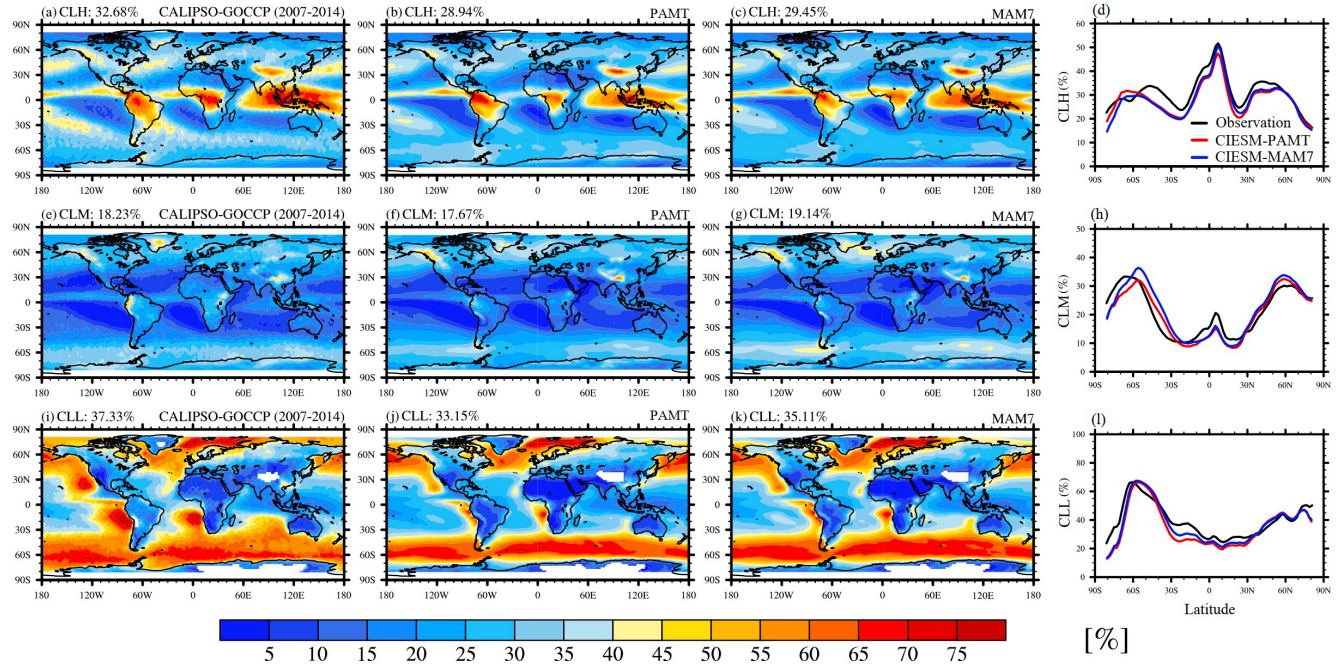


Figure 5. Spatial distribution and zonal-mean comparison of high, middle, and low cloud fractions (*CLH*, *CLM*, *CLL*) simulated by CIESM-PAMT/MAM7 with CALIPSO-GOCCP. Unit: %.

Figure 6 shows the spatial distribution and zonal mean variations of clouds in different phases (liquid and ice) as simulated by CIESM-PAMT and CIESM-MAM7. Overall, the two aerosol modules produce broadly consistent cloud distributions. Both underestimate liquid cloud fraction (*CLW*) by 9% and 2%, respectively, and overestimate ice cloud fraction (*CLI*) by 22% and 15%, with MAM7 generally showing better agreement with observations. The largest biases are concentrated in mid- to high-latitude regions, where *CLW* is underestimated and *CLI* is overestimated. Guo et al. (2020), using NCAR CESM1.2.1, analysed CIESM's simulation of clouds in different phases and reached similar conclusions—namely, that the fraction of supercooled liquid water was underestimated and the Wegener–Bergeron–Findeisen (WBF) process was too strong. Yang et al. (2025) and Xia et al. (2026) subsequently reduced these biases by improving the WBF process in the model.

Analysis of cloud fraction simulations indicates that, despite replacing the aerosol module in CIESM, there is little difference in cloud fraction between CIESM-PAMT and CIESM-MAM7. This is likely because cloud fraction is computed within the cloud macrophysics, which is not directly coupled to the aerosol module. In addition, the model simulations employed a Newtonian relaxation (nudging) approach to constrain the horizontal wind fields toward observations. As a result, the large-scale wind patterns in CIESM-PAMT and CIESM-MAM7 are very similar, which further diminishes the influence of aerosols on cloud fraction.

https://doi.org/10.5194/egusphere-2026-6624
Preprint. Discussion started: 10 November 2026
© Author(s) 2026. CC BY 4.0 License.

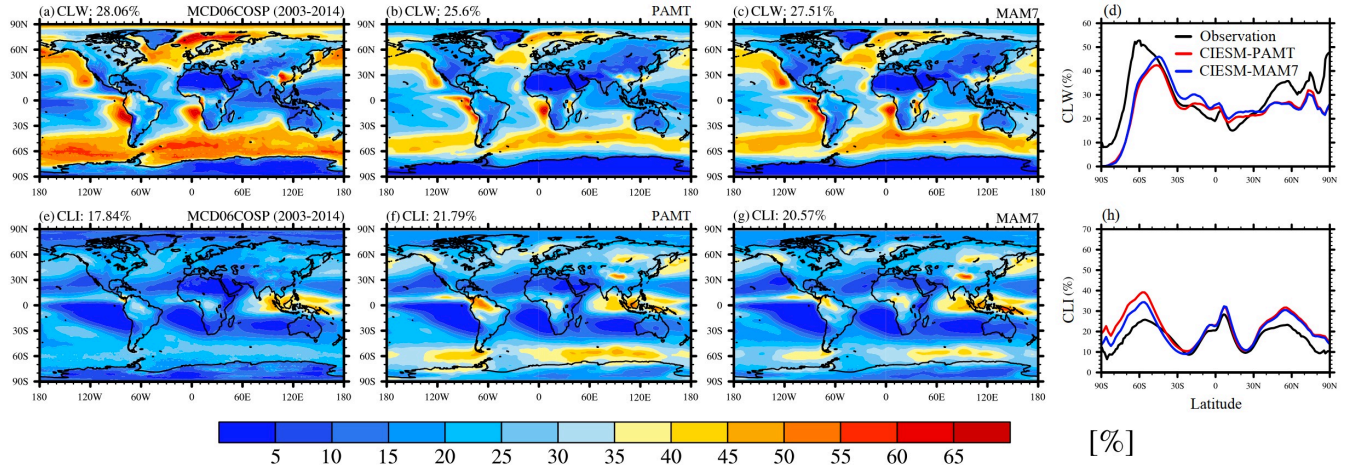


Figure 6. Spatial distribution and zonal-mean comparison of liquid and ice cloud fractions (*CLW*, *CLI*) simulated by CIESM-PAMT/MAM7 against MCD06COSP. Units: %.

According to the Twomey effect, under a given cloud water content, an increase in aerosol concentration leads to higher cloud droplet number concentration (N_d) and smaller cloud droplet effective radius (R_e), thereby enhancing cloud albedo (Twomey, 1977). Therefore, a realistic simulation of N_d is a prerequisite for accurately representing aerosol–cloud interactions.

Figure 7 shows the comparison of cloud-top N_d in large-scale liquid clouds simulated by CIESM-PAMT and CIESM-MAM7 against various observational datasets (Bennartz and Rausch, 2017; Grosvenor et al., 2018; Quaas et al., 2006; Zhu et al., 2018). Over the ocean, clouds are more likely to satisfy the adiabatic ascent assumption used in N_d retrievals (Painemal and Zuidema, 2011; Quaas and Gryspeerdt, 2022), making satellite-based N_d more reliable than over land. Accordingly, this study uses only the oceanic portion of the data for evaluation.

The results show that while the absolute N_d values differ among datasets, their spatial distributions are largely consistent: high N_d values are concentrated along continental coastlines, whereas low values dominate over the open ocean, a pattern that is also captured by CIESM simulations. Compared to MAM7, PAMT produces higher N_d values, with its zonal mean falling within the uncertainty range of the observational datasets (Fig. 7c). MAM7 tends to underestimate N_d relative to satellite observations and shows less pronounced latitudinal variation, failing to capture the higher values in the Northern Hemisphere and lower values in the Southern Hemisphere. Overall, CIESM-PAMT demonstrates superior performance in simulating N_d compared to CIESM-MAM7.

https://doi.org/10.5194/egusphere-2026-6624
Preprint. Discussion started: 10 November 2026
© Author(s) 2026. CC BY 4.0 License.

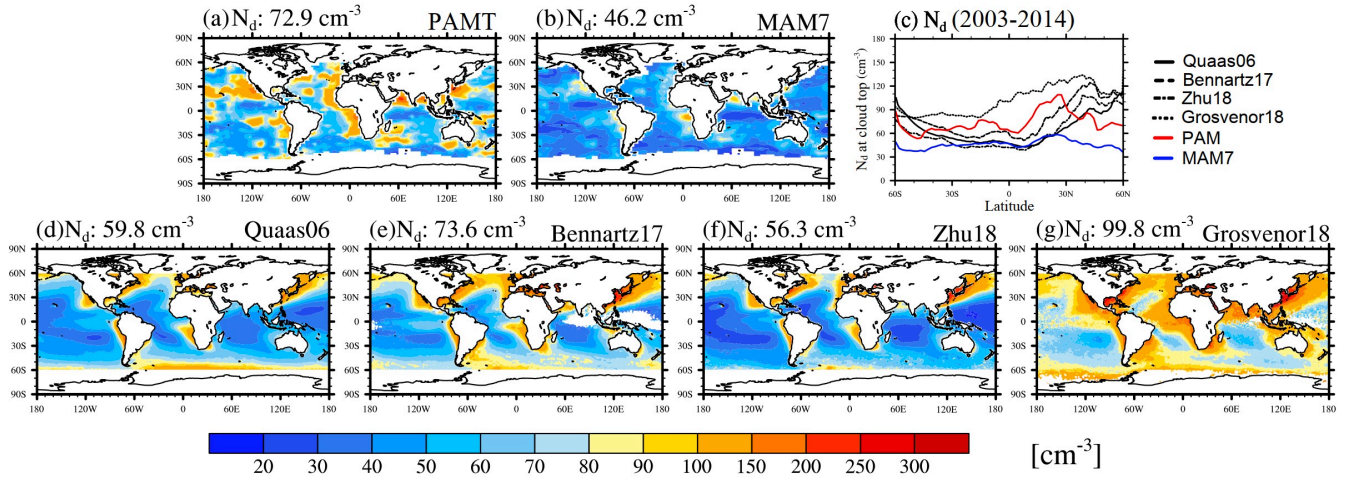


Figure 7. Spatial distribution and zonal-mean comparison of warm-cloud top droplet number concentration (N_d) simulated by CIESM-PAMT/MAM7 and retrieved using different methods. The retrieval approaches include (d–g) Quaas06, Bennartz16, Zhu18, and Grosvenor18. Unit: cm⁻³.

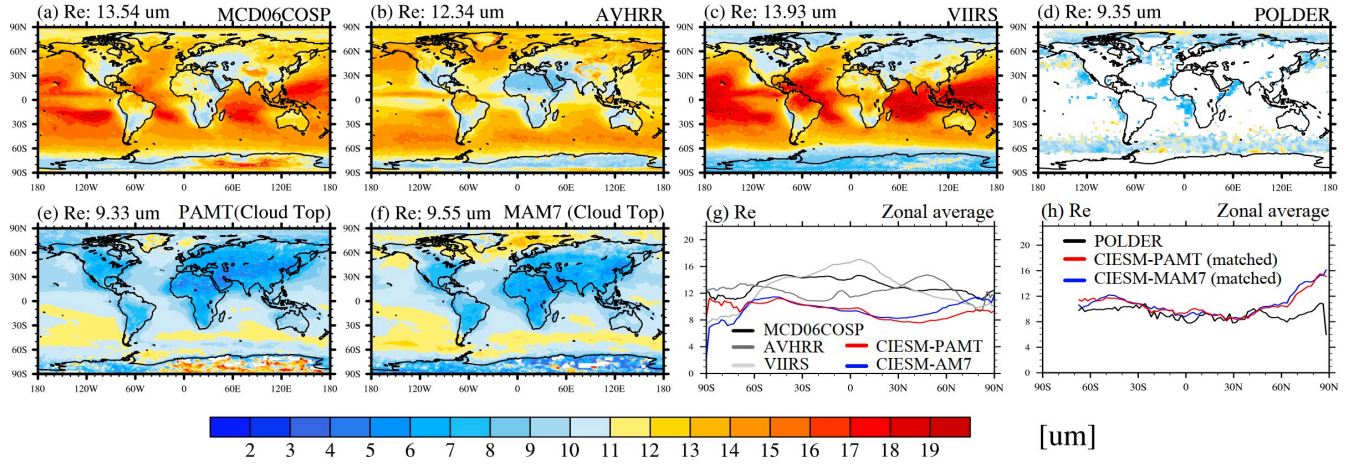


Figure 8. Spatial distribution and zonal-mean comparison of warm-cloud cloud-top droplet effective radius (R_e) from CIESM-PAMT/MAM7 simulations and satellite observations (MCD06COSP, AVHRR, VIIRS, and POLDER). Unit: μm.

Figure 8 presents a comparison of warm cloud cloud-top effective radius (R_e) simulated by CIESM with liquid cloud R_e derived from various satellite products, including MODIS, AVHRR, VIIRS, and POLDER. Overall, the global mean R_e from MODIS, AVHRR, and VIIRS is approximately 13 μm, which is generally higher than in-situ observations (Peng et al., 2002; Wang et al., 2022b). Rosenfeld et al. (2012) pointed out that the effective radius for cloud-to-rain transition is around 14 μm, indicating that the relatively high R_e from these satellites may imply the presence of substantial drizzle at cloud tops, potentially deviating from actual conditions. Shang et al. (2019) proposed an improved primary cloudbow retrieval (PCR) algorithm, which enhances the accuracy of R_e retrievals, especially for large droplets, and this dataset is also included in the CIESM evaluation (Fig. 8d). Compared with other satellites, R_e retrieved from POLDER in 2008 using polarization methods

https://doi.org/10.5194/egusphere-2026-6624
Preprint. Discussion started: 10 November 2026
© Author(s) 2026. CC BY 4.0 License.

is generally smaller. The CIESM-simulated R_e at cloud tops is shown in Figs. 8e–f, with the zonal mean comparison with observations presented in Figs. 8g–h. The results indicate that CIESM reproduces the spatial distribution and global mean of cloud-top R_e reasonably well, with relative bias below 5%. Compared with MODIS, AVHRR, and VIIRS, the model tends to underestimate R_e, although CIESM-PAMT agrees better with observations in the high southern latitudes, and CIESM-MAM7 aligns more closely in the mid-to-high northern latitudes. Comparisons with POLDER show generally good consistency, though R_e is slightly underestimated overall, particularly in mid-to-high latitudes. In summary, CIESM-simulated R_e falls within the range of R_e reported by current satellite-based observations.

Figure 9 presents CIESM-simulated and observed LWP. The observational reference is the MAC-LWP dataset (Elsaesser et al., 2017), which merges multiple sources to provide cloud water path data. Compared to this dataset, CIESM tends to overestimate LWP, particularly in subtropical and midlatitude regions. In Fig. 9a, the hatched areas indicate regions where retrievals have relative biases exceeding 10% for data merging, and the overestimation of CIESM in midlatitudes occurs outside these areas, indicating that the bias originates from the model itself rather than observational uncertainty. Comparing the PAMT and MAM7 simulations reveals notable differences in the Northern Hemisphere midlatitudes, with PAMT predicting substantially higher LWP than MAM7 (Fig. 9d). This arises because while both modules simulate similar R_e, PAMT predicts markedly higher N_d in this region (Fig. 8c). Since both simulations employ the same cloud-to-rain autoconversion parameterization (Khairoutdinov and Kogan, 2000), in which the autoconversion rate scales positively with cloud liquid water content and negatively with cloud droplet number concentration, the higher N_d in PAMT suppresses autoconversion and favors the retention of cloud liquid water, leading to the higher LWP.

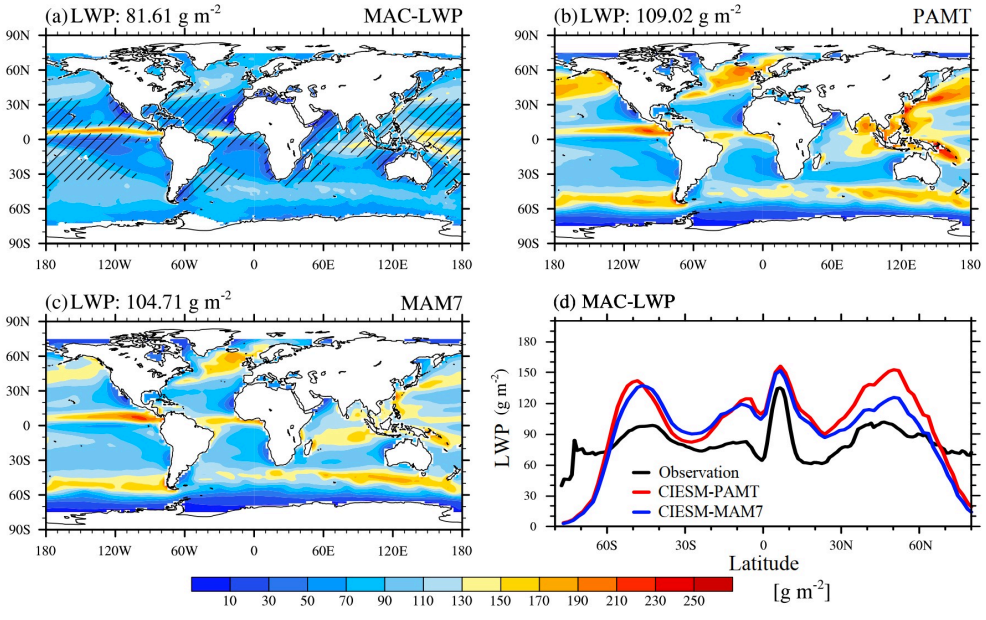


Figure 9. Spatial distribution and zonal-mean comparison of cloud liquid water path (LWP) from CIESM-PAMT/MAM7 simulations and the multi-sensor observational dataset MAC-LWP. In panel (a), the hatched regions indicate areas where the relative bias exceeds 10%. Unit: g m⁻².

https://doi.org/10.5194/egusphere-2026-6624
Preprint. Discussion started: 10 November 2026
© Author(s) 2026. CC BY 4.0 License.

Figure 10 presents the spatial distribution and zonal variation of *IWP* as simulated by CIESM compared with observations. The results indicate that PAMT and MAM7 produce similar *IWP* patterns, with high values concentrated in the tropics and midlatitudes, consistent with observations. However, CIESM significantly overestimates *IWP* in the Southern Ocean, with simulated values nearly double those observed (Fig. 10d). This overestimation may be related to the enhanced WBF process in the model, which promotes excessive ice crystal production (Guo et al., 2020; Yang et al., 2025). Further analysis is needed to identify the underlying causes of these *LWP* and *IWP* biases.

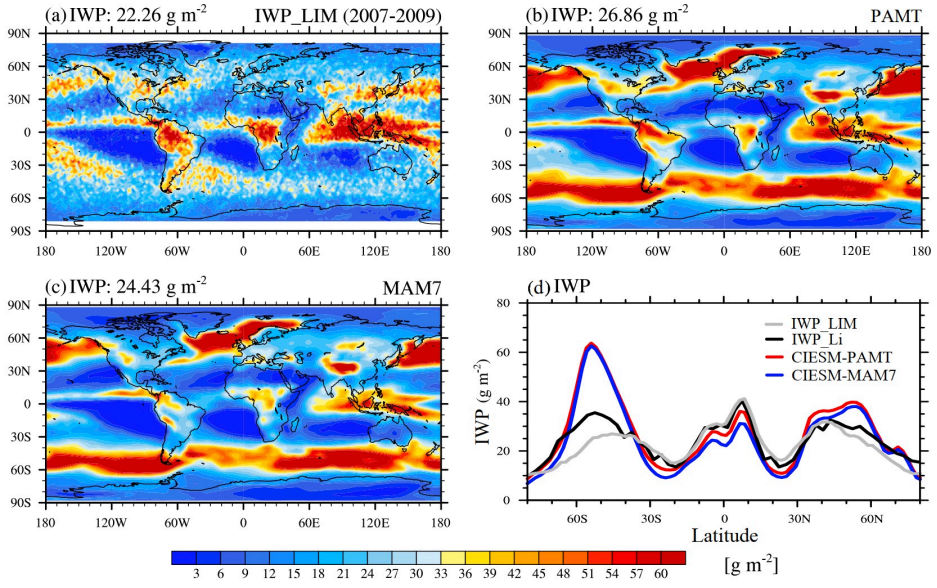


Figure 10. Spatial distribution and zonal-mean comparison of ice water path (*IWP*) from CIESM-PAMT/MAM7 simulations and observations. Unit: g m⁻².

Table 2. Comparison of cloud-related variables between CIESM-PAMT/MAM7 simulations and observations. Light green shading indicates better model performance. No annotation is applied when the simulation bias of the two models is less than 5%, indicating no significant difference.

Variable	CIESM-PAMT	CIESM-MAM7	Observation	Data source
$CCN02$	204.2	100.7	232.2	CCN_SAT
CLT [%]	54.1 (50.1 - 60.2)	55.6 (50.9 - 62.4)	65.8 (65.0 - 67.0)	CALIPSO-GOCCP, ISCCP, MCD06COSP
CLH [%]	28.9	29.5	32.7	CALIPSO-GOCCP
CLM [%]	17.7	19.1	18.2	CALIPSO-GOCCP
CLL [%]	33.2	35.1	37.3	CALIPSO-GOCCP
CLW [%]	25.6	27.5	28.1	MCD06COSP
CLI [%]	21.8	20.6	17.9	MCD06COSP
N_d [cm^{-3}]	72.9	46.2	72.4 (56.3 - 99.8)	Quaas06, Bennartz17, Grosvenor18, Zhu18
R_e [μm]	9.9	9.8	9.4 - 13.9	MODIS, AVHRR, VIIRS, POLDER
LWP [g m^{-2}]	109	104.7	81.6	MAC-LWP
IWP [g m^{-2}]	26.9	24.4	22.3	IWP_LIM

https://doi.org/10.5194/egusphere-2026-6624
Preprint. Discussion started: 10 November 2026
© Author(s) 2026. CC BY 4.0 License.

Table 2 summarizes the cloud simulation characteristics of CIESM-PAMT/MAM7. Overall, both PAMT and MAM7 produce broadly consistent results for most cloud properties, including cloud fraction, liquid water, and ice water, for which the differences between the two schemes are generally within 10%. In contrast, the differences in CCN and N_d are substantially larger, reaching approximately 50%. Specifically, MAM7 performs slightly better in simulating cloud fraction, whereas PAMT shows improved performance in representing cloud condensation nuclei and cloud droplet number concentration. In all other aspects, the differences between the two modules are minimal, with biases generally below 5%. These results highlight that the differences between the two modules are more pronounced in aerosol activation-related quantities than in bulk cloud properties.

4.3 Evaluation of Precipitation

Figure 11 presents the spatial distribution and zonal mean of total precipitation rate ($Prec$) simulated by CIESM-PAMT/MAM7, compared with observational data (GPCP and TRMM). Overall, CIESM reproduces the spatial patterns of precipitation reasonably well, with both high and low precipitation regions broadly consistent with observations, although the global mean tends to be slightly overestimated. Specifically, CIESM-PAMT shows a slightly closer agreement with observations, particularly near the equatorial regions, where it slightly reduces the precipitation intensity in the double Intertropical Convergence Zone (ITCZ) areas.

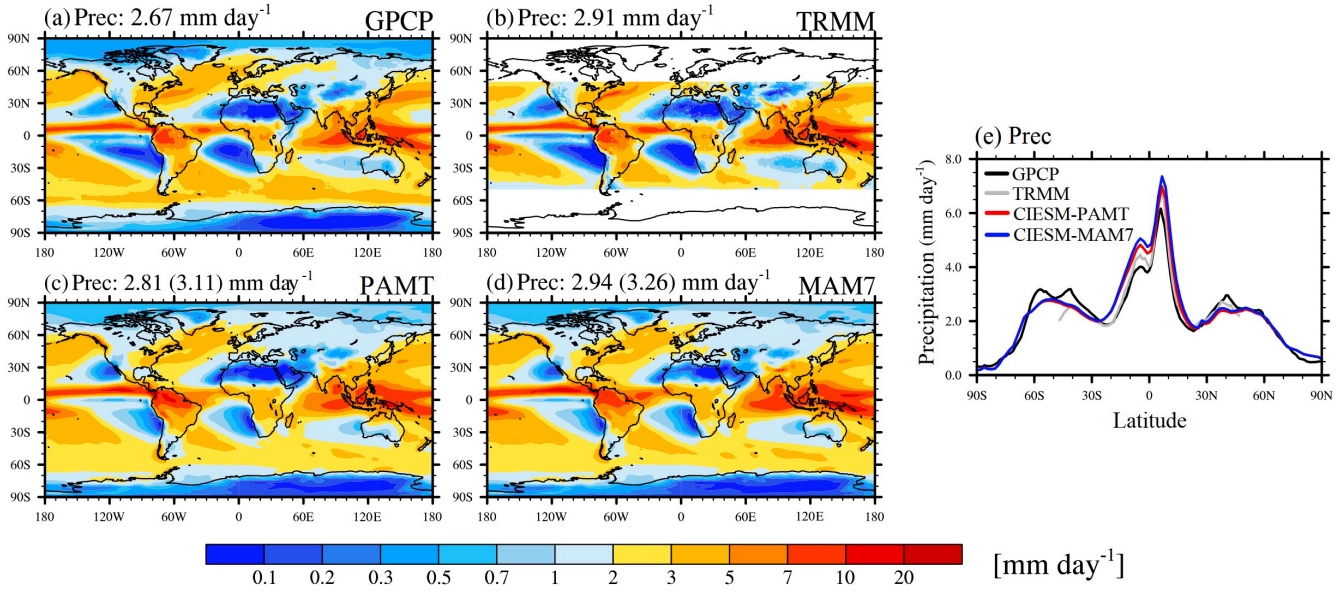


Figure 11. Spatial distribution and zonal-mean comparison of total precipitation rate ($Prec$) from CIESM-PAMT/MAM7 simulations compared with GPCC and TRMM observations. Values in parentheses indicate the global mean over the region corresponding to TRMM. Unit: mm day⁻¹.

https://doi.org/10.5194/egusphere-2026-6624
Preprint. Discussion started: 10 November 2026
© Author(s) 2026. CC BY 4.0 License.

4.4 Evaluation of Radiation

Figure 12 shows the shortwave (SW), longwave (LW), and net radiative fluxes (Net) at the top of atmosphere (TOA). On a global average, PAMT and MAM7 perform similarly, with relative biases for all variables remaining below 5%. Compared to CERES observations, both modules reproduce the global mean Net reasonably well, while LW and SW are slightly underestimated (relative bias around -1%), mainly over equatorial regions. The zonal mean analysis further confirms the good agreement: the zonal mean averages of radiative fluxes at TOA simulated by PAMT and MAM7 closely match the observations, with the curves nearly overlapping across all latitudes. This indicates that CIESM is capable of accurately reproducing radiative fluxes at TOA.

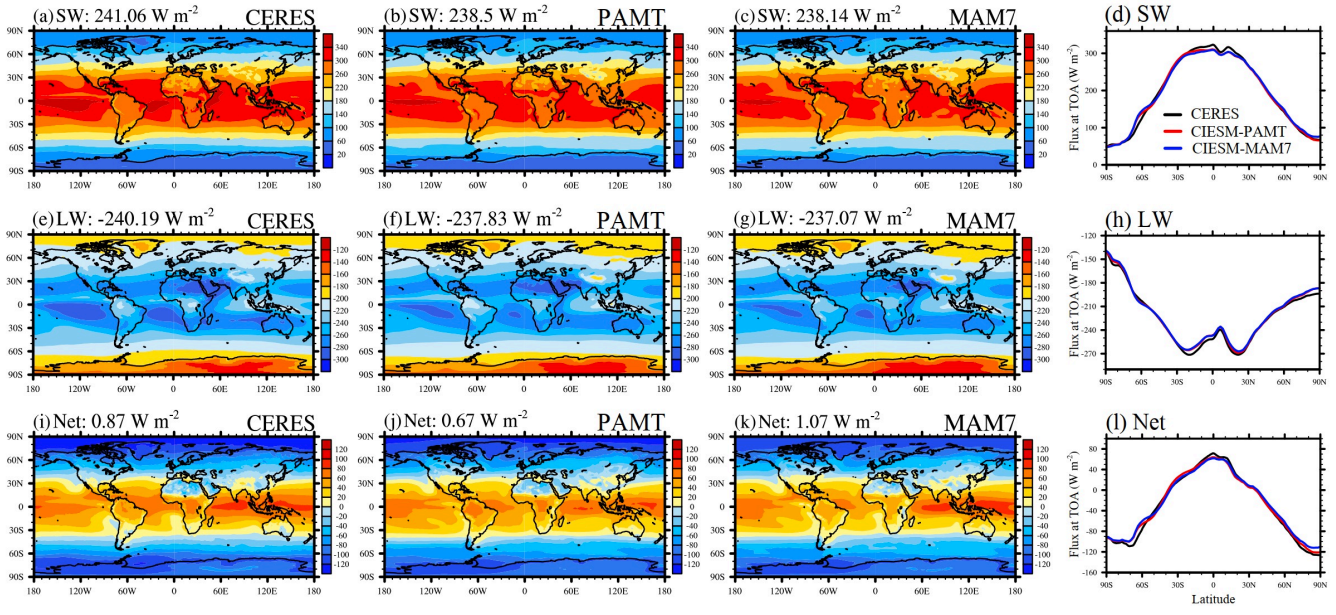


Figure 12. Spatial distribution and zonal-mean comparison of top-of-atmosphere shortwave (SW), longwave (LW), and net radiation fluxes (Net) from CIESM-PAMT/MAM7 simulations and CERES observations. Unit: W m⁻².

In addition, this study computed the shortwave, longwave, and net cloud radiative effects (denoted as SW_CRE, LW_CRE, and Net_CRE, respectively) using CIESM and compared the results with CERES satellite observations, as shown in Fig. 13. Despite the relatively good performance of CIESM in simulating radiative fluxes at TOA, CIESM exhibits substantial biases in cloud radiative effects, manifested as an overall overestimation of cloud-induced cooling (Figs. 13i-l). Specifically, the global-mean biases of SW_CRE, LW_CRE, and Net_CRE relative to observations are −7.7 W m⁻², −5.7 W m⁻², and −13.4 W m⁻² for PAMT, and −6.2 W m⁻², −7.6 W m⁻², and −13.8 W m⁻² for MAM7, respectively. These biases primarily originate from errors in simulated longwave cloud radiative fluxes (Fig. 13h), with systematically underestimated LW_CRE across latitudes, leading to an unrealistically weak cloud greenhouse effect. This tendency toward overly strong cloud radiative cooling is not unique to CIESM but is a common feature in many GCMs. For example, similar issues have been reported for NCAR CESM2 and ECHAM6.3–HAM2.3 in previous evaluations (Danabasoglu et al., 2020; Neubauer et al., 2019). In particular, evaluations

https://doi.org/10.5194/egusphere-2026-6624
Preprint. Discussion started: 10 November 2026
© Author(s) 2026. CC BY 4.0 License.

of NCAR CESM2 have shown that this bias can be partially alleviated by adjustments to deep convection schemes and mixed-phase cloud parameterizations in NCAR CESM1 (Danabasoglu et al., 2020). Nevertheless, the exact causes of the biases in CIESM remain unclear, and further targeted sensitivity experiments are required to elucidate the underlying mechanisms.

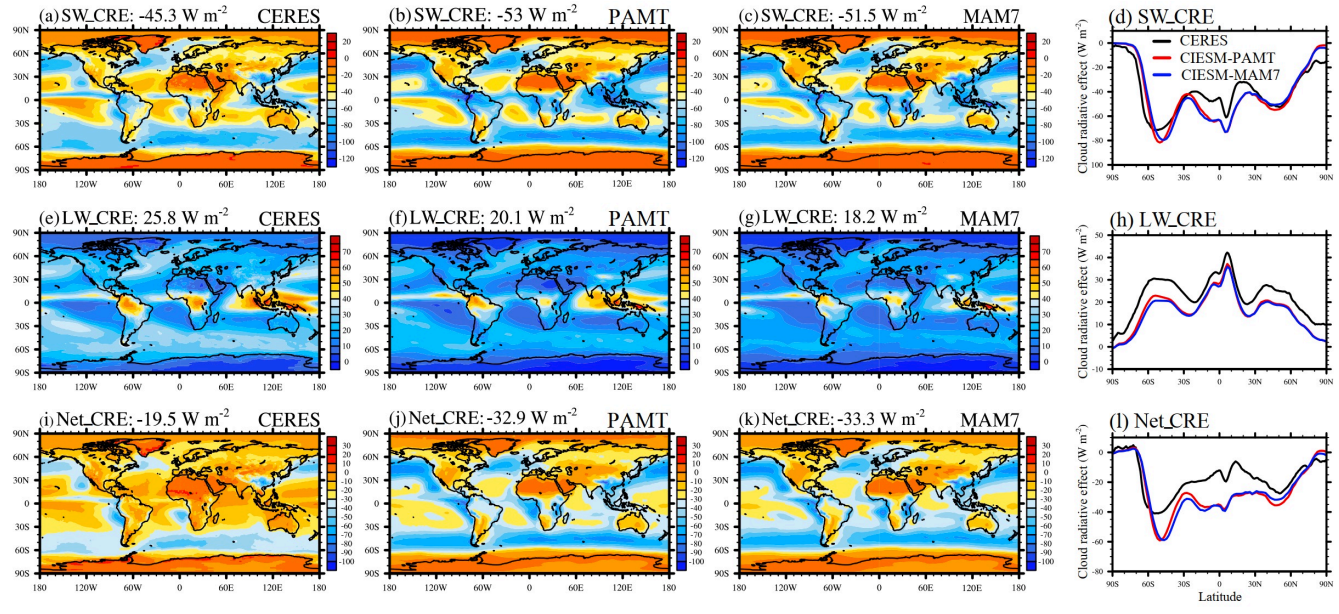


Figure 13. Spatial distribution and zonal-mean comparison of shortwave (*SW_CRE*), longwave (*LW_CRE*), and net cloud radiative effects (*Net_CRE*) from CIESM-PAMT/MAM7 simulations and CERES observations. Unit: W m^{-2}.

Table 3. Comparison of precipitation and radiation simulation results from CIESM-PAMT/MAM7 with observations. Light green shading indicates better model performance. No annotation is applied when the simulation bias of the two models is less than 5%, indicating no significant difference.

Variable		CIESM-PAMT	CIESM-MAM7	Observation	Data source
Precipitation [mm d^{-1}]	*Pre*	2.8	2.9	2.7	GPCC
	Pre (47°S − 47°N)	3.1	3.3	2.9	TRMM
Radiation [W m^{-2}]	*SW*	238.5	238.1	241.1 (238 - 244)	CERES range of uncertainty:(Loeb et al., 2009; Matus and L'Ecuyer, 2017; Stevens and Schwartz, 2012)
	LW	-237.8	-237.1	-240.2 (-237 - -241)	
	Net	0.67	1.07	0.87	
	SW_CRE	-53.0	-51.5	-45.3 (-44 - 53.3)	
	LW_CRE	20.1	18.2	25.8 (22 - 30.5)	
	Net_CRE	-32.9	-33.3	-19.5 (-17.1 - 22.8)	

A summary of the precipitation and radiation simulations by CIESM-PAMT and CIESM-MAM7 is presented in Table 3. Overall, PAMT and MAM7 show only small differences in simulated precipitation rates and radiative fluxes, with relative biases generally within 5%. In more detail, PAMT performs slightly better than MAM7 in reproducing precipitation rates. For top-of-atmosphere radiative fluxes, PAMT and MAM7 exhibit similar skill, and both fall within the observational uncertainty

https://doi.org/10.5194/egusphere-2026-6624
Preprint. Discussion started: 10 November 2026
© Author(s) 2026. CC BY 4.0 License.

range. In contrast, both modules show relatively large biases in simulated cloud radiative effects compared with observations. The simulated SW_CRE has a larger magnitude but remains within the observational uncertainty, whereas the LW_CRE and Net_CRE fall outside the observed ranges. Overall, PAMT shows marginally better performance than MAM7.

4.5 Evaluation of Aerosol–cloud Interactions

In this study, the partial radiative perturbation (PRP) method was used to quantify the radiative forcing associated with different ACI effects simulated by CIESM-PAMT/MAM7 (Mülmenstädt et al., 2019), including F_{N_d}, F_{ql}, F_{fcl}, F_{N_i}, F_{qi}, and F_{fci} (see Section 2.4). A description of the PRP method is provided in the Appendix A.

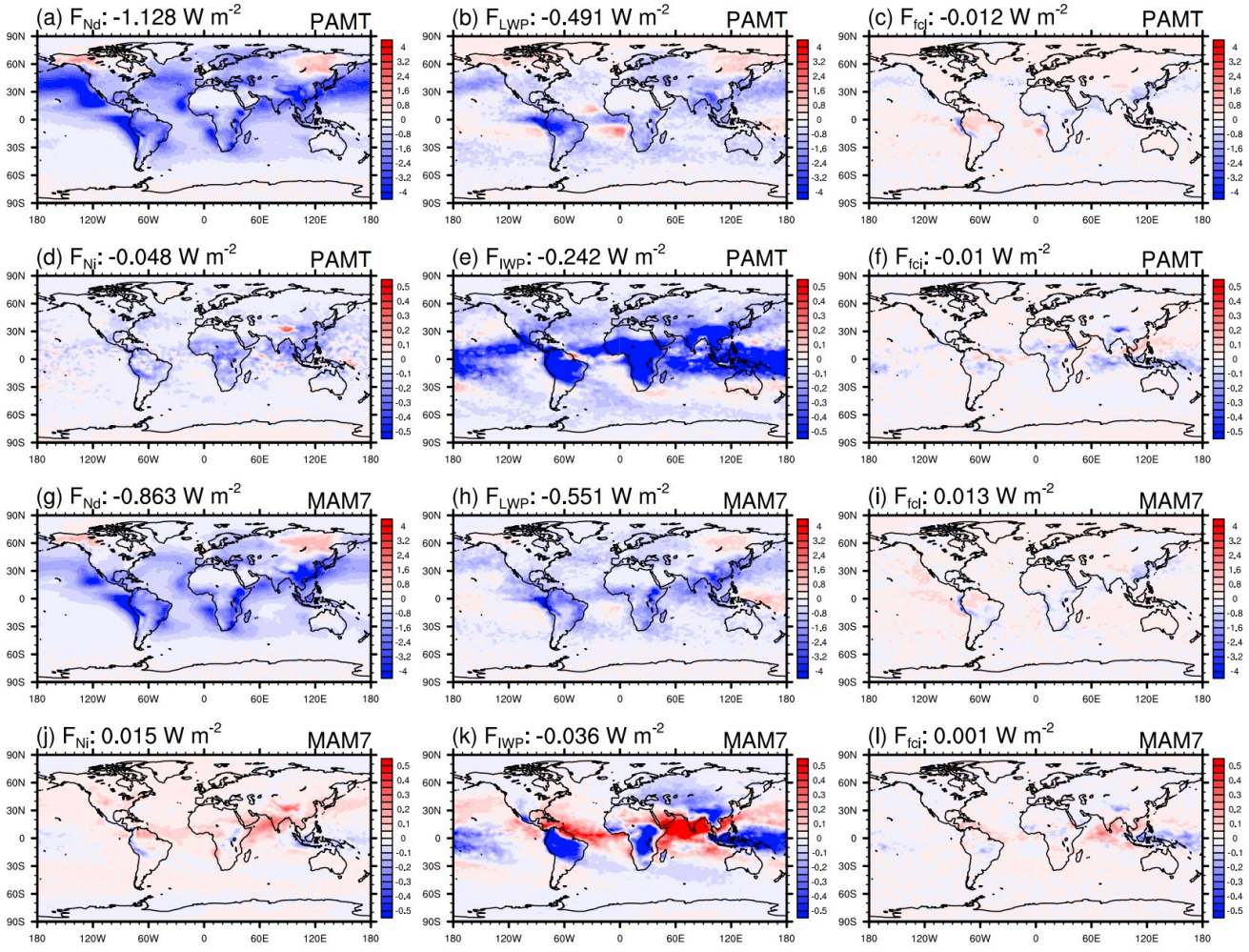


Figure 14. Radiative forcing of different ACI components calculated by CIESM-PAMT/MAM7 using the PRP method. Note that the ranges of color bar differ for liquid and ice clouds. Unit: W m-2.

As shown in Fig. 14, the results indicate that CIESM-PAMT produces a stronger total ACI radiative forcing than CIESM-MAM7 (PAMT: −1.9 W m^{-2}; MAM7: −1.4 W m^{-2}), particularly for the radiative forcing associated with the Twomey effect

https://doi.org/10.5194/egusphere-2026-6624
Preprint. Discussion started: 10 November 2026
© Author(s) 2026. CC BY 4.0 License.

(PAMT: −1.1 W m^{-2}; MAM7: −0.9 W m^{-2}). Based on observational constraints summarized in IPCC AR6 (IPCC, 2023), the estimated total ACI radiative forcing and the Twomey-effect-related forcing are −1.0 ± 0.7 W m−2 (medium confidence) and −0.7 ± 0.5 W m−2 (medium confidence), respectively, suggesting that CIESM tends to overestimate the magnitude of ACI, leading to an overly strong cooling effect. However, Jia et al. (2021) noted that satellite-based estimates of ACI are often weaker than model-based estimates, which is consistent with our results. For rapid adjustments of liquid water path and cloud fraction, PAMT and MAM7 produce similar results (Figs. 14b–c, h–i). In contrast, substantial differences are found in the simulation of aerosol–ice cloud effects. CIESM-PAMT simulates a predominantly negative aerosol–ice cloud radiative effect, whereas CIESM-MAM7 produces a predominantly positive effect. The underlying causes of this discrepancy require further investigation. IPCC AR6 highlighted the large uncertainties in aerosol effects on ice clouds, including uncertainty in the sign of the effect itself, which is consistent with the findings of this study.

To provide a more comprehensive assessment of the simulated Twomey effect, the results from CIESM were compared with those reported in Jia et al. (2021), as shown in Fig. 15. The results indicate that the radiative forcing of Twomey effect (F_{N_d}) simulated by CIESM is generally biased low relative to observations, implying a stronger cooling effect, particularly in the CIESM-PAMT configuration (Fig. 15b). The underestimation is most pronounced in regions strongly influenced by anthropogenic aerosols, such as coastal continental regions, the North Pacific, East Asia, and India (Figs. 15c-d). In terms of spatial patterns, the CIESM-PAMT simulation shows better agreement with observations, exhibiting a consistent meridional structure characterized by a decrease from low to mid-latitudes followed by an increase toward higher latitudes, with a minimum around 45° N (Fig. 15b). In contrast, CIESM-MAM7 tends to underestimate F_{N_d} in low latitudes while overestimating it in mid-latitudes, leading to partial compensation of the biases and a global mean that appears more consistent with observations, but with poorer spatial fidelity compared to CIESM-PAMT. However, both CIESM-PAMT and CIESM-MAM7 substantially underestimate F_{N_d} south of 35° S (Fig. 15b). We suspect that this bias may be related to our prescribed minimum N_d of 30 cm^{-3}, which warrants further investigation and optimization in future work.

Furthermore, model–observation comparisons were conducted across 14 global regions defined by Quaas et al. (2008), and the results are summarized in Table 4. The comparison indicates that CIESM-PAMT performs better than CIESM-MAM7 in a larger number of regions (8 vs. 5), particularly over midlatitude regions in both hemispheres and extensive oceanic areas.

https://doi.org/10.5194/egusphere-2026-6624
Preprint. Discussion started: 10 November 2026
© Author(s) 2026. CC BY 4.0 License.

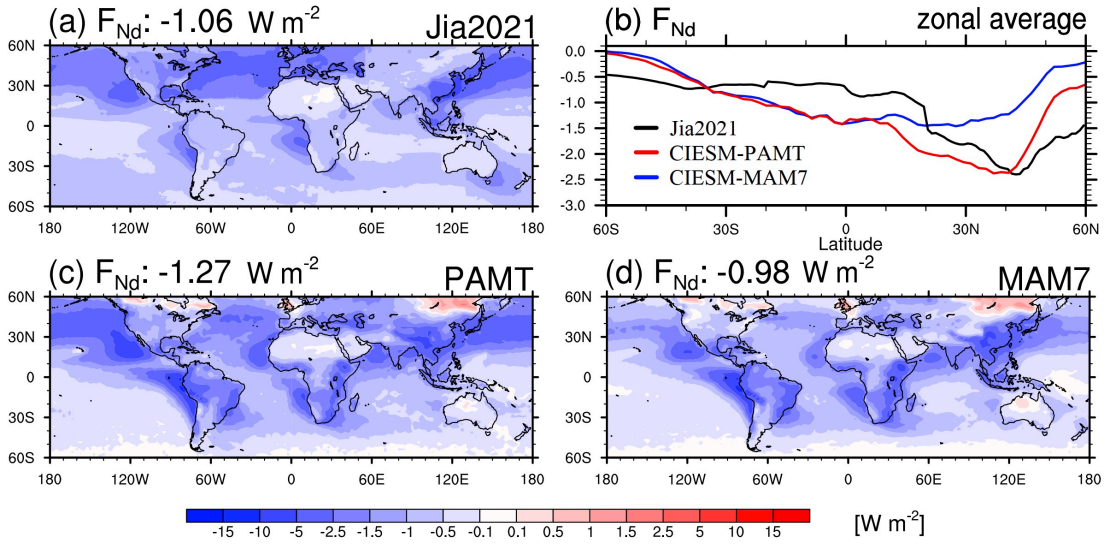


Figure 15. Radiative forcing due to the Twomey effect (F_{N_d}) calculated by CIESM-PAMT/MAM7 using the PRP method, along with its spatial distribution and zonal mean comparison with results from Jia et al. (2021). Unit: W m^{-2}.

Table 4. Comparison of CIESM-PAMT/MAM7 simulated radiative forcing due to the Twomey effect with observational data. Light green shading indicates better model performance. No annotation is applied when the simulation bias of the two models is less than 5%, indicating no significant difference.

Region		CIESM-PAMT	CIESM-MAM7	Jia2021
North Pacific Ocean		-2.91	-1.35	-2.41
North America		-0.99	-0.69	-1.27
North Atlantic Ocean		-1.7	-1.06	-2.75
Europe		-1.42	-1.17	-1.87
Asia		-1.64	-1.28	-1.02
Tropical Pacific Ocean		-1.23	-0.99	-0.73
Tropical Atlantic Ocean		-1.33	-1.19	-1.04
Africa		-1.21	-1.39	-0.46
Tropical Indian Ocean		-1.19	-1.11	-0.65
South Pacific Ocean		-0.38	-0.35	-0.75
South America		-1.78	-1.83	-0.69
South Atlantic Ocean		-0.81	-0.71	-0.60
South Indian Ocean		-0.53	-0.49	-0.59
Australia		-0.37	-0.36	-0.41
Ocean (60S-60N)	Northern Hemisphere	-2.00	-1.21	-1.71
	Southern Hemisphere	-0.68	-0.63	-0.65
	All	-1.24	-0.87	-1.10
Global (60S-60N)	Northern Hemisphere	-1.72	-1.17	-1.49
	Southern Hemisphere	-0.83	-0.80	-0.64
	All	-1.27	-0.98	-1.06

https://doi.org/10.5194/egusphere-2026-6624
Preprint. Discussion started: 10 November 2026
© Author(s) 2026. CC BY 4.0 License.

In addition, we analysed F_{N_d} separately over the mid- to low-latitudes (60°S–60°N) for both the global (land + ocean) and ocean-only domains, and calculated the hemispheric values for the Northern Hemisphere (NH) and Southern Hemisphere (SH). The SH–NH contrast in F_{N_d} has received considerable attention because N_d over the pristine SH have been proposed as a suitable proxy for preindustrial conditions (McCoy et al., 2020). However, many global climate models tend to overestimate ACI in the SH, likely because the preindustrial atmosphere is simulated as being too clean owing to underestimated natural CCN sources, such as biomass burning and biogenic VOCs emissions (Carslaw et al., 2013; Wang et al., 2025b). In CIESM, however, the SH F_{N_d} simulated by PAMT and MAM7 is very similar (the relative bias less than 5%). In particular, the ocean-only F_{N_d} over the SH is in excellent agreement with the observation-based estimate (Table 4), which is likely attributable to the prescribed lower bound of N_d in the model. Referring to Jia and Quaas (2023), we imposed a minimum N_d of 30 cm^{-3}, as observations indicate that N_d does not approach zero even under extremely low aerosol loading. Similar lower-bound constraints have also been adopted in other global climate models; for example, ECHAM6.3-HAM2.3 prescribes minimum N_d values of 20 or 40 cm^{-3}, depending on the model configuration (Neubauer et al., 2019). Moreover, the observation-based estimates exhibit a pronounced hemispheric contrast, with NH F_{N_d} being approximately 2.5 times larger than that in the SH. CIESM-PAMT successfully reproduces this hemispheric contrast, whereas CIESM-MAM7 substantially underestimates it (Table 4).

Overall, CIESM-PAMT provides a more realistic representation of F_{N_d} and better captures the radiative forcing induced by the Twomey effect associated with anthropogenic aerosols.

5 Conclusions

Building on the aerosol evaluation presented in Part 1 of this study, we systematically assessed the performance of the new-generation integrated aerosol–climate model CIESM-PAMT in simulating clouds, precipitation, radiation, and aerosol–cloud interactions (ACI), and compared it with the original CIESM-MAM7 configuration. The results show that, after introducing a more detailed sectional size distribution, updated representations of aerosol sources and sinks, and a more physically consistent aerosol activation scheme (QDGE), CIESM-PAMT more accurately simulates cloud condensation nuclei and cloud droplet number concentrations, thereby providing a stronger foundation for ACI studies. Further analysis indicates that, relative to CIESM-MAM7, CIESM-PAMT exhibits better spatial consistency with satellite observations in simulating Twomey-effect-induced radiative forcing, demonstrating a clear improvement in its ACI representation. However, CIESM-PAMT does not show a clear advantage in cloud fraction simulations, and its performance in effective droplet radius, liquid and ice water paths, and radiation-related variables remains comparable to that of CIESM-MAM7. These results should be interpreted with caution, as the differences between CIESM-PAMT and CIESM-MAM7 in cloud and radiation variables are relatively small compared with the overall model biases. Although differences in aerosol representation and activation can affect cloud and radiative properties, these variables are also influenced by other physical processes. Therefore, the differences between the two

https://doi.org/10.5194/egusphere-2026-6624
Preprint. Discussion started: 10 November 2026
© Author(s) 2026. CC BY 4.0 License.

configurations do not necessarily imply an overall improvement in cloud and radiation simulations, but rather reflect the impacts of the aerosol scheme on the coupled aerosol–cloud–radiation system. This suggests that the influence of the aerosol scheme is most clearly reflected in cloud droplet number concentration, whereas its effects on other cloud properties are less pronounced and may be modulated by additional physical processes and cannot be attributed solely to the aerosol scheme.

In addition, this study successfully implemented the partial radiative perturbation (PRP) method into CIESM, enabling the model to isolate different components of ACI, including the Twomey effect, cloud water path adjustments, cloud fraction adjustments, and multiple radiative forcing components associated with ice clouds. The introduction of this capability not only enhances the physical interpretability of ACI mechanisms within the model, but also provides a technical foundation for developing a radiative forcing diagnostic framework that can be directly compared with satellite observations. This approach is expected to help more tightly constrain the long-standing uncertainties associated with ACI in GCMs. Nevertheless, the current analysis of radiative forcing contributions from different ACI components remains relatively limited, and more in-depth investigations are required.

Taken together with the aerosol performance reported in Part 1, CIESM-PAMT demonstrates strong skill in coupled aerosol–cloud–radiation simulations, improving the physical consistency and interpretability of aerosol–cloud–radiation interactions in CIESM. The model shows enhanced capability in capturing the spatial distribution and optical properties of aerosols, as well as in representing cloud droplet number concentrations and the Twomey effect, thus providing a solid foundation for future ACI simulations.

The evaluation framework and diagnostic system developed in this study point to several priorities for future model development: 1) improving the simulation of cloud fraction, particularly for different cloud phases; 2) conducting targeted experiments to investigate the causes of large liquid water path biases, especially in mid-latitude regions, and improving the representation of hydrometeors in the cloud macrophysics scheme; 3) performing sensitivity experiments to identify the sources of biases in simulated effective cloud radiative effects, with particular attention to longwave cloud radiative effects; conducting a trend analysis of model-simulated aerosols and related processes; 4) further investigating why the total ACI radiative forcing simulated by CIESM-PAMT, despite showing good agreement with F_{N_d} and Jia2021, appears stronger than the range reported in IPCC AR6; 5) exploring the causes of the opposite signs in the global-mean aerosol–ice cloud radiative effects derived from PAMT and MAM7 using the PRP method; 6) and considering the role of aerosol–deep convective cloud interactions in future ACI analyses, given that convective microphysics is already represented in CIESM but is often neglected in current ACI diagnostics, including in the present study.

Overall, this study provides the first systematic and comprehensive evaluation of CIESM-PAMT, and establishes a solid scientific foundation for its future participation in international comparison projects and broader aerosol–climate interaction research. With continued improvements in the physical representation of aerosol and cloud microphysical processes, CIESM-PAMT has the potential to play an increasingly important role in reducing aerosol-related uncertainties in global climate assessments, improving the simulation of climate feedbacks, and enhancing the predictive capability for extreme weather events.

https://doi.org/10.5194/egusphere-2026-6624
Preprint. Discussion started: 10 November 2026
© Author(s) 2026. CC BY 4.0 License.

Appendix A: Partial Radiative Perturbations

To separate the radiative forcing contributions from different components of aerosol–cloud interactions (ACI) in climate models, Mülmenstädt et al. (2019) introduced the Partial Radiative Perturbations (PRP) method. The workflow of the method applied in CIESM is shown in Fig. A1.

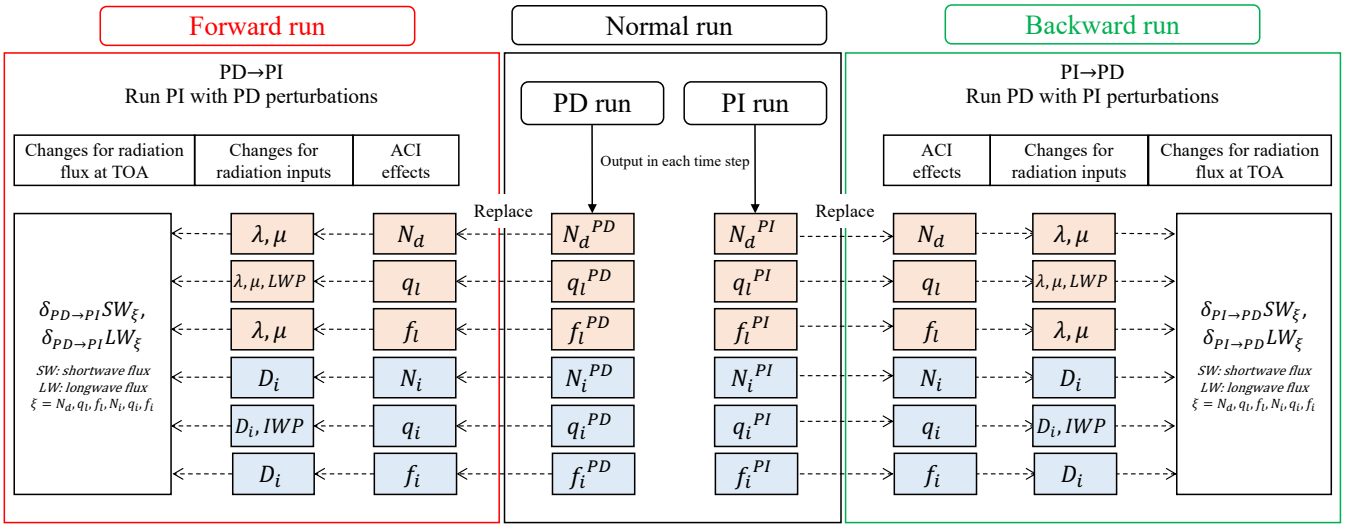


Figure A1. Schematic diagram of the Partial Radiative Perturbations (PRP) method. PI denotes the pre-industrial period (1850), PD denotes the present-day period (2010), N_d and N_i are the cloud droplet and ice crystal number concentrations, q_l and q_i are the cloud liquid water and cloud ice water contents, f_l and f_i are the liquid-cloud and ice-cloud fractions, δ represents the difference, λ and μ are cloud droplet spectral parameters used in the model, LWP is the liquid water path, IWP is the ice water path, and D_i is the effective diameter of ice crystals.

Following the definition of ACI, the effective radiative forcing associated with anthropogenic aerosol changes (F_{aci}) can be expressed as the sum of the radiative forcing contributions from various aerosol-related effects:

$$F_{aci} = F_{N_d} + F_{q_l} + F_{f_l} + F_{N_i} + F_{q_i} + F_{f_i}\,, \tag{A1}$$

where F_{N_d} represents the radiative forcing associated with the Twomey effect; F_{q_l} and F_{f_l} correspond to the radiative forcing resulting from adjustments in liquid water path (LWP) and cloud fraction, respectively. Similarly, F_{N_i} denotes the radiative forcing driven by increases in ice-nucleating aerosols, while F_{q_i} and F_{f_i} represent the radiative forcing associated with adjustments in ice water path (IWP) and ice cloud fraction. Considering the correspondence with variables on the model's three-dimensional grid, the model representations for the different effects—$N_d, q_l, f_l, N_i, q_i, f_i$—respectively denote cloud droplet number concentration, cloud liquid water content, liquid cloud fraction, ice crystal number concentration, ice water content, and ice cloud fraction. For convenience in model calculations, concentration variables are typically converted to mixing ratios by dividing by the dry air density. Other adjustments, such as surface temperature changes or temperature and humidity adjustments within the atmosphere, have been shown to produce radiative effects that are generally small and therefore often neglected (Heyn et al., 2017).

https://doi.org/10.5194/egusphere-2026-6624
Preprint. Discussion started: 10 November 2026
© Author(s) 2026. CC BY 4.0 License.

In the PRP experiments, the first step is to run the PI and PD simulations normally (i.e., the normal run in Fig. A1) and store, at every time step, the cloud microphysical variables relevant to ACI, denoted as $\boldsymbol{x}^{PI}$ and $\boldsymbol{x}^{PD}$, where $\boldsymbol{x} = \{N_d, q_l, f_l, N_i, q_i, f_i\}$. Next, a set of forward and backward experiments is performed. Using the forward experiment as an example—specifically, running the PI simulation while replacing individual PI variables with their PD counterparts (i.e., forward run in Fig. A1)—we describe the detailed procedure for computing the change in net shortwave flux.

In the second step, six PI simulations are conducted in the forward experiment, each targeting one cloud microphysical variable. In each simulation, the radiative transfer module is invoked using the double-call method. For illustration, consider the experiment isolating the N_d effect (i.e., Twomey effect). During the first call to the radiation module, the model computes the TOA net shortwave flux under PI conditions, noted as SW^{PI}. During the second call, N_d diagnosed by the model is replaced, at every time step, with the corresponding PD value stored from the normal experiment ($\boldsymbol{x}^{PD}$), while all other cloud variables remain unchanged. The resulting TOA net shortwave flux is denoted as $SW^{PI}\left(\left\{\boldsymbol{x}_{\xi}^{PD}, \boldsymbol{x}_{\zeta\neq\xi}^{PI}\right\}\right)$. Here, the braces denote the set of variables used in the radiative calculation; the subscript ξ marks the perturbed variable (e.g., ${N_d}^{PD}$ in the calculation of N_d effect), while the remaining variables are marked with $\zeta \neq \xi$. The difference between the two TOA shortwave fluxes computed in the double call yields the shortwave radiative forcing associated with the PI→PD increase in N_d, that is, the Twomey-effect shortwave forcing, denoted $\delta_{PD\to PI}SW_{N_d}$. Repeating the same double-call procedure for each of the six cloud microphysical variables produces six distinct shortwave radiative forcing components attributable to anthropogenic aerosol increases (as shown in the forward run of Fig. A1), thereby isolating the individual contributions of each aerosol effect.

$$\delta_{PD\to PI}SW_{\xi} = SW^{PI}\left(\left\{x_{\xi}^{PD}, x_{\zeta\neq\xi}^{PI}\right\}\right) - SW^{PI}\ , \tag{A2}$$

The third step follows a procedure analogous to the second step, but using six double-call radiative calculations within the PD simulations. In each experiment, when replacing a cloud microphysical variable, the corresponding value from $\boldsymbol{x}^{PI}$—stored during the first step—is used to overwrite the normally computed PD variable. This procedure yields the shortwave radiative forcing associated with the reduction of anthropogenic aerosols (from PD to PI) through the changes in each cloud microphysical variable, as illustrated in the backward run of Fig. A1.

$$\delta_{PI\to PD}SW_{\xi} = SW^{PD}\left(\left\{x_{\xi}^{PI}, x_{\zeta\neq\xi}^{PD}\right\}\right) - SW^{PD}\ , \tag{A3}$$

The same three-step procedure is also applied to the TOA net longwave radiation flux (denoted as LW). This allows the calculation of the longwave radiative forcing associated with each cloud microphysical variable due to anthropogenic aerosol increases or decreases (from PI to PD / from PD to PI), denoted as $\delta_{PD\to PI}LW_{\xi}$ and $\delta_{PI\to PD}LW_{\xi}$, respectively. In this way, the six individual aerosol effects on longwave radiative forcing are separated.

In practice, the PRP method perturbs the radiative flux calculations without interfering with the model's dynamical run, i.e., it relies on the double-call approach when invoking the radiation module. Since N_d is not a direct input to the radiation module, cloud microphysical parameters λ and μ must be computed prior to the module call. Different cloud variables affect the inputs

https://doi.org/10.5194/egusphere-2026-6624
Preprint. Discussion started: 10 November 2026
© Author(s) 2026. CC BY 4.0 License.

to the radiation module in distinct ways: for example, N_d and q_l influence the cloud droplet spectrum parameters λ and μ, q_l also affects LWP, while N_i and q_i influence the ice crystal effective diameter D_i, and q_i also affects IWP, as illustrated in Fig. A1.

When running forward or backward experiments individually, changing only a single variable can sometimes produce unrealistic results—for example, a grid cell may contain no cloud while the substituted N_d is nonzero, representing a nonphysical decoupling of cloud variables. (Mülmenstädt et al., 2019) showed that averaging the forward and backward δ values effectively mitigate this issue, preventing spurious signals from biasing the assessment of radiative effects. Consequently, the shortwave radiative forcing caused by aerosol-induced changes in a given cloud microphysical variable can be expressed as

$$\delta_{PI\leftrightarrow PD}SW_\xi = \frac{\delta_{PD\rightarrow PI}SW_\xi - \delta_{PI\rightarrow PD}SW_\xi}{2}, \tag{A4}$$

with a similar formulation applying for longwave radiation. Using the PRP method, the radiative forcing attributable to aerosol effects through a specific cloud microphysical variable can be represented as

$$F_\xi = \delta_{PI\leftrightarrow PD}SW_\xi + \delta_{PI\leftrightarrow PD}LW_\xi , \tag{A5}$$

where $\xi = N_d$, q_l, f_l, N_i, q_i and f_i corresponds to F_{N_d}, F_{q_l}, F_{f_l}, F_{N_i}, F_{q_i} and F_{f_i}, respectively.

Code and data availability. The CIESM source code is publicly available at http://doi.org/10.5281/zenodo.3596317 (YishuangLiang and hxmhuang, 2020) , and documentation for the PAM can be accessed at https://gitlab.com/PAMdev/canam5.1-pam and described by https://cccma.gitlab.io/PAM/PAMcode.html. The CCN_SITE and CCN_MOD datasets are available at https://doi.org/10.5281/zenodo.3265866, and the CCN_SAT dataset can be obtained from https://doi.pangaea.de/10.1594/PANGAEA.956215. The MCD06COSP dataset is available at https://ladsweb.modaps.eosdis.nasa.gov/archive/allData/62/MCD06COSP_M3_MODIS/, and the CALIPSO-GOCCP dataset can be accessed at https://climserv.ipsl.polytechnique.fr/cfmip-obs/. MODIS, ISCCP, AVHRR, and GPCP products are available from the ICDC data portal at https://www.cen.uni-hamburg.de/en/icdc/data/atmosphere. The datasets of cloud droplet number concentration (Quaas06, Bennartz17, Zhu18, and Grosvenor18) can be obtained from https://catalogue.ceda.ac.uk/uuid/864a46cc65054008857ee5bb772a2a2b/. The MAC-LWP dataset is available at https://disc.gsfc.nasa.gov/datasets/MACTWP_mean_1/summary?keywords=MAC-LWP, and the TRMM dataset can be accessed at https://disc.gsfc.nasa.gov/datasets/TRMM_3B43_7/summary?keywords=trmm. CERES data are available from https://asdc.larc.nasa.gov/project/CERES. The IWP_LIM and Jia2021 datasets are available from the corresponding authors upon reasonable request. Last accessed: 1 December, 2025.

https://doi.org/10.5194/egusphere-2026-6624
Preprint. Discussion started: 10 November 2026
© Author(s) 2026. CC BY 4.0 License.

Author contribution. HW processed the datasets, performed the simulations and analyses, and wrote the manuscript. YP conceived and led the study and designed the experiments. KVS provided the PAM code and guidance on model coupling and evaluation. HL, HS, DJ, XH, and JQ contributed to the acquisition and use of satellite datasets, while JQ also guided the assessment of aerosol–cloud interactions. MW provided guidance on model coupling and evaluation. JL generated the aerosol optical property lookup tables using Mie scattering. HJ provided the Jia2021 dataset and guidance on its application. YW provided the CCN dataset over China and guidance on its application. LF guided the accurate description of PAMT. YP, KVS, HL, and JQ supervised the project and revised the manuscript. All authors contributed to the final manuscript.

Competing interests. The authors declare that they have no conflict of interest.

Acknowledgements. This work is supported by the National Key Research and Development Program of China (2024YFB3907900, 2024YFB390870101, 2024YFB3908300), the European Union Horizon Europe project “CleanCloud” (101137639), and the National Key Scientific and Technological Infrastructure project “Earth System Numerical Simulation Facility” (EarthLab). This work also utilized resources of the German Climate Computing Centre (Deutsches Klimarechenzentrum, DKRZ) provided under project ID 1143 by its Scientific Steering Committee (WLA).

Financial support. This work has been supported by the National Key Research and Development Program of China (grant no. 2024YFB3907900).

https://doi.org/10.5194/egusphere-2026-6624
Preprint. Discussion started: 10 November 2026
© Author(s) 2026. CC BY 4.0 License.

References

Abdul-Razzak, H. and Ghan, S. J.: A parameterization of aerosol activation: 2. Multiple aerosol types, Journal of Geophysical Research: Atmospheres, 105, 6837–6844, https://doi.org/10.1029/1999JD901161, 2000.

Albrecht, B. A.: Aerosols, Cloud Microphysics, and Fractional Cloudiness, Science (1979)., 245, 1227–1230, https://doi.org/10.1126/science.245.4923.1227, 1989.

AMAP: AMAP Assessment 2021: Impacts of Short-lived Climate Forcers on Arctic Climate, Air Quality, and Human Health, Arctic Monitoring and Assessment Programme (AMAP), x + 375pp p., https://www.amap.no/documents/doc/amap-assessment-2021-impacts-of-short-lived-climate-forcers-on-arctic-climate-air-quality-and-human-health/3614, 2021.

Barth, M. C., Rasch, P. J., Kiehl, J. T., Benkovitz, C. M., and Schwartz, S. E.: Sulfur chemistry in the National Center for Atmospheric Research Community Climate Model: Description, evaluation, features, and sensitivity to aqueous chemistry, Journal of Geophysical Research: Atmospheres, 105, 1387–1415, https://doi.org/10.1029/1999JD900773, 2000.

Bellouin, N., Quaas, J., Gryspeerdt, E., Kinne, S., Stier, P., Watson-Parris, D., Boucher, O., Carslaw, K. S., Christensen, M., Daniau, A. -L., Dufresne, J. -L., Feingold, G., Fiedler, S., Forster, P., Gettelman, A., Haywood, J. M., Lohmann, U., Malavelle, F., Mauritsen, T., McCoy, D. T., Myhre, G., Mülmenstädt, J., Neubauer, D., Possner, A., Rugenstein, M., Sato, Y., Schulz, M., Schwartz, S. E., Sourdeval, O., Storelvmo, T., Toll, V., Winker, D., and Stevens, B.: Bounding Global Aerosol Radiative Forcing of Climate Change, Reviews of Geophysics, 58, https://doi.org/10.1029/2019RG000660, 2020.

Bennartz, R. and Rausch, J.: Global and regional estimates of warm cloud droplet number concentration based on 13 years of AQUA-MODIS observations, Atmos. Chem. Phys., 17, 9815–9836, https://doi.org/10.5194/acp-17-9815-2017, 2017.

Bevan, S. L., North, P. R. J., Los, S. O., and Grey, W. M. F.: A global dataset of atmospheric aerosol optical depth and surface reflectance from AATSR, Remote Sens. Environ., 116, 199–210, https://doi.org/10.1016/j.rse.2011.05.024, 2012.

Binkowski, F. S. and Roselle, S. J.: Models-3 Community Multiscale Air Quality (CMAQ) model aerosol component 1. Model description, Journal of Geophysical Research: Atmospheres, 108, https://doi.org/10.1029/2001JD001409, 2003.

Binkowski, F. S. and Shankar, U.: The Regional Particulate Matter Model: 1. Model description and preliminary results, Journal of Geophysical Research: Atmospheres, 100, 26191–26209, https://doi.org/10.1029/95JD02093, 1995.

Bodas-Salcedo, A., Webb, M. J., Bony, S., Chepfer, H., Dufresne, J.-L., Klein, S. A., Zhang, Y., Marchand, R., Haynes, J. M., Pincus, R., and John, V. O.: COSP: Satellite simulation software for model assessment, Bull. Am. Meteorol. Soc., 92, 1023–1043, https://doi.org/10.1175/2011BAMS2856.1, 2011.

Carslaw, K. S., Lee, L. A., Reddington, C. L., Pringle, K. J., Rap, A., Forster, P. M., Mann, G. W., Spracklen, D. V., Woodhouse, M. T., Regayre, L. A., and Pierce, J. R.: Large contribution of natural aerosols to uncertainty in indirect forcing, Nature, 503, 67–71, https://doi.org/10.1038/nature12674, 2013.

Chepfer, H., Bony, S., Winker, D., Cesana, G., Dufresne, J. L., Minnis, P., Stubenrauch, C. J., and Zeng, S.: The GCM-Oriented CALIPSO Cloud Product (CALIPSO-GOCCP), Journal of Geophysical Research: Atmospheres, 115, D00H16, https://doi.org/10.1029/2009JD012251, 2010.

https://doi.org/10.5194/egusphere-2026-6624
Preprint. Discussion started: 10 November 2026
© Author(s) 2026. CC BY 4.0 License.

Chin, M., Wright, J. S., Bian, H., Tan, Q., Pan, X., Takemura, T., Matsui, H., Tsigaridis, K., Bauer, S., Ginoux, P., Peng, Y., Guo, Z., Fadnavis, S., Laakso, A., Burrows, J. P., Taha, G., Kar, J., Rozanov, A., Arosio, C., Rieger, L., and Bourassa, A.: Variability and trends of upper-tropospheric aerosols over the Asian summer monsoon region: an AeroCom multi-model study, Atmos. Chem. Phys., 26, 6035–6059, https://doi.org/10.5194/ACP-26-6035-2026, 2026.

Choudhury, G. and Tesche, M.: Estimating cloud condensation nuclei concentrations from CALIPSO lidar measurements, Atmos. Meas. Tech., 15, 639–654, https://doi.org/10.5194/amt-15-639-2022, 2022.

Choudhury, G. and Tesche, M.: A first global height-resolved cloud condensation nuclei data set derived from spaceborne lidar measurements, Earth Syst. Sci. Data, 15, 3747–3760, https://doi.org/10.5194/essd-15-3747-2023, 2023.

Croft, B., Lohmann, U., and von Salzen, K.: Black carbon ageing in the Canadian Centre for Climate modelling and analysis atmospheric general circulation model, Atmos. Chem. Phys., 5, 1931–1949, https://doi.org/10.5194/acp-5-1931-2005, 2005.

Croft, B., Lohmann, U., Martin, R. V., Stier, P., Wurzler, S., Feichter, J., Posselt, R., and Ferrachat, S.: Aerosol size-dependent below-cloud scavenging by rain and snow in the ECHAM5-HAM, Atmos. Chem. Phys., 9, 4653–4675, https://doi.org/10.5194/acp-9-4653-2009, 2009.

d'Almeida, G. A. , K. P. S. E. P.: Atmospheric aerosols : Global climatology and radiative characteristics, A. Deepak Pub., Hampton, VA, https://api.semanticscholar.org/CorpusID:127815484, 1991.

Danabasoglu, G., Lamarque, J. -F., Bacmeister, J., Bailey, D. A., DuVivier, A. K., Edwards, J., Emmons, L. K., Fasullo, J., Garcia, R., Gettelman, A., Hannay, C., Holland, M. M., Large, W. G., Lauritzen, P. H., Lawrence, D. M., Lenaerts, J. T. M., Lindsay, K., Lipscomb, W. H., Mills, M. J., Neale, R., Oleson, K. W., Otto-Bliesner, B., Phillips, A. S., Sacks, W., Tilmes, S., van Kampenhout, L., Vertenstein, M., Bertini, A., Dennis, J., Deser, C., Fischer, C., Fox-Kemper, B., Kay, J. E., Kinnison, D., Kushner, P. J., Larson, V. E., Long, M. C., Mickelson, S., Moore, J. K., Nienhouse, E., Polvani, L., Rasch, P. J., and Strand, W. G.: The Community Earth System Model Version 2 (CESM2), J. Adv. Model. Earth Syst., 12, https://doi.org/10.1029/2019MS001916, 2020.

Delanoë, J. and Hogan, R. J.: A variational scheme for retrieving ice cloud properties from combined radar, lidar, and infrared radiometer, Journal of Geophysical Research: Atmospheres, 113, 7204, https://doi.org/10.1029/2007JD009000, 2008.

Deschamps, P.-Y., Breon, F.-M., Leroy, M., Podaire, A., Bricaud, A., Buriez, J.-C., and Seze, G.: The POLDER mission: instrument characteristics and scientific objectives, IEEE Transactions on Geoscience and Remote Sensing, 32, 598–615, https://doi.org/10.1109/36.297978, 1994.

Doktorowski, S., Kretzschmar, J., Quaas, J., Salzmann, M., and Sourdeval, O.: Subgrid-scale variability of cloud ice in the ICON-AES 1.3.00, Geosci. Model Dev., 17, 3099–3110, https://doi.org/10.5194/gmd-17-3099-2024, 2024.

Dunne, E. M., Gordon, H., Kürten, A., Almeida, J., Duplissy, J., Williamson, C., Ortega, I. K., Pringle, K. J., Adamov, A., Baltensperger, U., Barmet, P., Benduhn, F., Bianchi, F., Breitenlechner, M., Clarke, A., Curtius, J., Dommen, J., Donahue, N. M., Ehrhart, S., Flagan, R. C., Franchin, A., Guida, R., Hakala, J., Hansel, A., Heinritzi, M., Jokinen, T., Kangasluoma, J., Kirkby, J., Kulmala, M., Kupc, A., Lawler, M. J., Lehtipalo, K., Makhmutov, V., Mann, G., Mathot, S., Merikanto, J., Miettinen, P., Nenes, A., Onnela, A., Rap, A., Reddington, C. L. S., Riccobono, F., Richards, N. A. D., Rissanen, M. P., Rondo,

https://doi.org/10.5194/egusphere-2026-6624
Preprint. Discussion started: 10 November 2026
© Author(s) 2026. CC BY 4.0 License.

L., Sarnela, N., Schobesberger, S., Sengupta, K., Simon, M., Sipilä, M., Smith, J. N., Stozkhov, Y., Tomé, A., Tröstl, J., Wagner, P. E., Wimmer, D., Winkler, P. M., Worsnop, D. R., and Carslaw, K. S.: Global atmospheric particle formation from CERN CLOUD measurements, Science (1979)., 354, 1119–1124, https://doi.org/10.1126/science.aaf2649, 2016.

Easter, R. C., Ghan, S. J., Zhang, Y., Saylor, R. D., Chapman, E. G., Laulainen, N. S., Abdul-Razzak, H., Leung, L. R., Bian, X., and Zaveri, R. A.: MIRAGE: Model description and evaluation of aerosols and trace gases, Journal of Geophysical Research: Atmospheres, 109, 20210, https://doi.org/10.1029/2004JD004571, 2004.

Elsaesser, G. S., O'Dell, C. W., Lebsock, M. D., Bennartz, R., Greenwald, T. J., and Wentz, F. J.: The Multisensor Advanced Climatology of Liquid Water Path (MAC-LWP), J. Clim., 30, 10193–10210, https://doi.org/10.1175/JCLI-D-16-0902.1, 2017.

Emerson, E. W., Hodshire, A. L., DeBolt, H. M., Bilsback, K. R., Pierce, J. R., McMeeking, G. R., and Farmer, D. K.: Revisiting particle dry deposition and its role in radiative effect estimates, Proceedings of the National Academy of Sciences, 117, 26076–26082, https://doi.org/10.1073/pnas.2014761117, 2020.

Emmons, L. K., Walters, S., Hess, P. G., Lamarque, J.-F., Pfister, G. G., Fillmore, D., Granier, C., Guenther, A., Kinnison, D., Laepple, T., Orlando, J., Tie, X., Tyndall, G., Wiedinmyer, C., Baughcum, S. L., and Kloster, S.: Description and evaluation of the Model for Ozone and Related chemical Tracers, version 4 (MOZART-4), Geosci. Model Dev., 3, 43–67, https://doi.org/10.5194/gmd-3-43-2010, 2010.

Eyring, V., Bony, S., Meehl, G. A., Senior, C. A., Stevens, B., Stouffer, R. J., and Taylor, K. E.: Overview of the Coupled Model Intercomparison Project Phase 6 (CMIP6) experimental design and organization, Geosci. Model Dev., 9, 1937–1958, https://doi.org/10.5194/gmd-9-1937-2016, 2016.

Fanourgakis, G. S., Kanakidou, M., Nenes, A., Bauer, S. E., Bergman, T., Carslaw, K. S., Grini, A., Hamilton, D. S., Johnson, J. S., Karydis, V. A., Kirkevåg, A., Kodros, J. K., Lohmann, U., Luo, G., Makkonen, R., Matsui, H., Neubauer, D., Pierce, J. R., Schmale, J., Stier, P., Tsigaridis, K., van Noije, T., Wang, H., Watson-Parris, D., Westervelt, D. M., Yang, Y., Yoshioka, M., Daskalakis, N., Decesari, S., Gysel-Beer, M., Kalivitis, N., Liu, X., Mahowald, N. M., Myriokefalitakis, S., Schrödner, R., Sfakianaki, M., Tsimpidi, A. P., Wu, M., and Yu, F.: Evaluation of global simulations of aerosol particle and cloud condensation nuclei number, with implications for cloud droplet formation, Atmos. Chem. Phys., 19, 8591–8617, https://doi.org/10.5194/acp-19-8591-2019, 2019.

Gettelman, A., Liu, X., Barahona, D., Lohmann, U., and Chen, C.: Climate impacts of ice nucleation, Journal of Geophysical Research: Atmospheres, 117, https://doi.org/10.1029/2012JD017950, 2012.

Ghan, S. J.: Technical Note: Estimating aerosol effects on cloud radiative forcing, Atmos. Chem. Phys., 13, 9971–9974, https://doi.org/10.5194/acp-13-9971-2013, 2013.

Ghan, S. J. and Zaveri, R. A.: Parameterization of optical properties for hydrated internally mixed aerosol, Journal of Geophysical Research: Atmospheres, 112, https://doi.org/10.1029/2006JD007927, 2007.

Glotfelty, T., He, J., and Zhang, Y.: Improving organic aerosol treatments in CESM/CAM5: Development, application, and evaluation, J. Adv. Model. Earth Syst., 9, 1506–1539, https://doi.org/10.1002/2016MS000874, 2017.

https://doi.org/10.5194/egusphere-2026-6624
Preprint. Discussion started: 10 November 2026
© Author(s) 2026. CC BY 4.0 License.

Grosvenor, D. P., Sourdeval, O., Zuidema, P., Ackerman, A., Alexandrov, M. D., Bennartz, R., Boers, R., Cairns, B., Chiu, J. C., Christensen, M., Deneke, H., Diamond, M., Feingold, G., Fridlind, A., Hünerbein, A., Knist, C., Kollias, P., Marshak, A., McCoy, D., Merk, D., Painemal, D., Rausch, J., Rosenfeld, D., Russchenberg, H., Seifert, P., Sinclair, K., Stier, P., van Diedenhoven, B., Wendisch, M., Werner, F., Wood, R., Zhang, Z., and Quaas, J.: Remote Sensing of Droplet Number Concentration in Warm Clouds: A Review of the Current State of Knowledge and Perspectives, Reviews of Geophysics, 56, 409–453, https://doi.org/10.1029/2017RG000593, 2018.

Gryspeerdt, E., Mülmenstädt, J., Gettelman, A., Malavelle, F. F., Morrison, H., Neubauer, D., Partridge, D. G., Stier, P., Takemura, T., Wang, H., Wang, M., and Zhang, K.: Surprising similarities in model and observational aerosol radiative forcing estimates, Atmos. Chem. Phys., 20, 613–623, https://doi.org/10.5194/acp-20-613-2020, 2020.

Gryspeerdt, E., McCoy, D. T., Crosbie, E., Moore, R. H., Nott, G. J., Painemal, D., Small-Griswold, J., Sorooshian, A., and Ziemba, L.: The impact of sampling strategy on the cloud droplet number concentration estimated from satellite data, Atmos. Meas. Tech., 15, 3875–3892, https://doi.org/10.5194/amt-15-3875-2022, 2022.

Guo, Z., Wang, M., Peng, Y., and Luo, Y.: Evaluation on the Vertical Distribution of Liquid and Ice Phase Cloud Fraction in Community Atmosphere Model Version 5.3 using Spaceborne Lidar Observations, Earth and Space Science, 7, https://doi.org/10.1029/2019EA001029, 2020.

Hanson, D. R.: Mass Accommodation of H2SO4 and CH3SO3H on Water−Sulfuric Acid Solutions from 6% to 97% RH, J. Phys. Chem. A, 109, 6919–6927, https://doi.org/10.1021/jp0510443, 2005.

Hersbach, H., Bell, B., Berrisford, P., Hirahara, S., Horányi, A., Muñoz-Sabater, J., Nicolas, J., Peubey, C., Radu, R., Schepers, D., Simmons, A., Soci, C., Abdalla, S., Abellan, X., Balsamo, G., Bechtold, P., Biavati, G., Bidlot, J., Bonavita, M., De Chiara, G., Dahlgren, P., Dee, D., Diamantakis, M., Dragani, R., Flemming, J., Forbes, R., Fuentes, M., Geer, A., Haimberger, L., Healy, S., Hogan, R. J., Hólm, E., Janisková, M., Keeley, S., Laloyaux, P., Lopez, P., Lupu, C., Radnoti, G., de Rosnay, P., Rozum, I., Vamborg, F., Villaume, S., and Thépaut, J.: The ERA5 global reanalysis, Quarterly Journal of the Royal Meteorological Society, 146, 1999–2049, https://doi.org/10.1002/qj.3803, 2020.

Heyn, I., Block, K., Mülmenstädt, J., Gryspeerdt, E., Kühne, P., Salzmann, M., and Quaas, J.: Assessment of simulated aerosol effective radiative forcings in the terrestrial spectrum, Geophys. Res. Lett., 44, 1001–1007, https://doi.org/10.1002/2016GL071975, 2017.

Hoesly, R. M., Smith, S. J., Feng, L., Klimont, Z., Janssens-Maenhout, G., Pitkanen, T., Seibert, J. J., Vu, L., Andres, R. J., Bolt, R. M., Bond, T. C., Dawidowski, L., Kholod, N., Kurokawa, J., Li, M., Liu, L., Lu, Z., Moura, M. C. P., O'Rourke, P. R., and Zhang, Q.: Historical (1750–2014) anthropogenic emissions of reactive gases and aerosols from the Community Emissions Data System (CEDS), Geosci. Model Dev., 11, 369–408, https://doi.org/10.5194/gmd-11-369-2018, 2018.

Holben, B. N.: Characteristics of maximum-value composite images from temporal AVHRR data, Int. J. Remote Sens., 7, 1417–1434, https://doi.org/10.1080/01431168608948945, 1986.

https://doi.org/10.5194/egusphere-2026-6624
Preprint. Discussion started: 10 November 2026
© Author(s) 2026. CC BY 4.0 License.

Hourdin, F., Mauritsen, T., Gettelman, A., Golaz, J.-C., Balaji, V., Duan, Q., Folini, D., Ji, D., Klocke, D., Qian, Y., Rauser, F., Rio, C., Tomassini, L., Watanabe, M., and Williamson, D.: The Art and Science of Climate Model Tuning, Bull. Am. Meteorol. Soc., 98, 589–602, https://doi.org/10.1175/BAMS-D-15-00135.1, 2017.

Huang, X., Tang, Q., Tseng, Y., Hu, Y., Baker, A. H., Bryan, F. O., Dennis, J., Fu, H., and Yang, G.: P-CSI v1.0, an accelerated barotropic solver for the high-resolution ocean model component in the Community Earth System Model v2.0, Geosci. Model Dev., 9, 4209–4225, https://doi.org/10.5194/gmd-9-4209-2016, 2016.

Hubanks, P., Pincus, R., Platnick, S., and Meyer, K.: MODIS (Aqua/Terra) Cloud Properties Level 3 monthly, 1x1 degree grid - LAADS DAAC, https://doi.org/10.5067/MODIS/MCD06COSP_M3_MODIS.062, 2023.

Huffman, G. J., Adler, R. F., Arkin, P., Chang, A., Ferraro, R., Gruber, A., Janowiak, J., McNab, A., Rudolf, B., and Schneider, U.: The Global Precipitation Climatology Project (GPCP) Combined Precipitation Dataset, Bull. Am. Meteorol. Soc., 78, 5–20, https://doi.org/10.1175/1520-0477(1997)078<0005:TGPCPG>2.0.CO;2, 1997.

Huffman, G. J., Bolvin, D. T., Nelkin, E. J., Wolff, D. B., Adler, R. F., Gu, G., Hong, Y., Bowman, K. P., and Stocker, E. F.: The TRMM Multisatellite Precipitation Analysis (TMPA): Quasi-Global, Multiyear, Combined-Sensor Precipitation Estimates at Fine Scales, J. Hydrometeorol., 8, 38–55, https://doi.org/10.1175/JHM560.1, 2007.

Huffman, G. J., Adler, R. F., Bolvin, D. T., and Gu, G.: Improving the global precipitation record: GPCP Version 2.1, Geophys. Res. Lett., 36, L17808, https://doi.org/10.1029/2009GL040000, 2009.

Hurrell, J. W., Holland, M. M., Gent, P. R., Ghan, S., Kay, J. E., Kushner, P. J., Lamarque, J.-F., Large, W. G., Lawrence, D., Lindsay, K., Lipscomb, W. H., Long, M. C., Mahowald, N., Marsh, D. R., Neale, R. B., Rasch, P., Vavrus, S., Vertenstein, M., Bader, D., Collins, W. D., Hack, J. J., Kiehl, J., and Marshall, S.: The Community Earth System Model: A Framework for Collaborative Research, Bull. Am. Meteorol. Soc., 94, 1339–1360, https://doi.org/10.1175/BAMS-D-12-00121.1, 2013.

Iacono, M. J., Delamere, J. S., Mlawer, E. J., Shephard, M. W., Clough, S. A., and Collins, W. D.: Radiative forcing by long-lived greenhouse gases: Calculations with the AER radiative transfer models, Journal of Geophysical Research: Atmospheres, 113, 13103, https://doi.org/10.1029/2008JD009944, 2008.

IPCC: The Earth's Energy Budget, Climate Feedbacks and Climate Sensitivity, in: Climate Change 2021 – The Physical Science Basis, Cambridge University Press, 923–1054, https://doi.org/10.1017/9781009157896.009, 2023.

Jia, H. and Quaas, J.: Nonlinearity of the cloud response postpones climate penalty of mitigating air pollution in polluted regions, Nat. Clim. Chang., 13, 943–950, https://doi.org/10.1038/s41558-023-01775-5, 2023.

Jia, H., Ma, X., Yu, F., and Quaas, J.: Significant underestimation of radiative forcing by aerosol–cloud interactions derived from satellite-based methods, Nat. Commun., 12, 3649, https://doi.org/10.1038/s41467-021-23888-1, 2021.

Jin, Z., Qiao, Y., Wang, Y., Fang, Y., and Yi, W.: A new parameterization of spectral and broadband ocean surface albedo, Opt. Express, 19, 26429, https://doi.org/10.1364/OE.19.026429, 2011.

Justice, C. O., Román, M. O., Csiszar, I., Vermote, E. F., Wolfe, R. E., Hook, S. J., Friedl, M., Wang, Z., Schaaf, C. B., Miura, T., Tschudi, M., Riggs, G., Hall, D. K., Lyapustin, A. I., Devadiga, S., Davidson, C., and Masuoka, E. J.: Land and cryosphere

https://doi.org/10.5194/egusphere-2026-6624
Preprint. Discussion started: 10 November 2026
© Author(s) 2026. CC BY 4.0 License.

products from Suomi NPP VIIRS: Overview and status, Journal of Geophysical Research: Atmospheres, 118, 9753–9765, https://doi.org/10.1002/jgrd.50771, 2013.

Kato, S., Loeb, N. G., Rose, F. G., Doelling, D. R., Rutan, D. A., Caldwell, T. E., Yu, L., and Weller, R. A.: Surface Irradiances Consistent with CERES-Derived Top-of-Atmosphere Shortwave and Longwave Irradiances, J. Clim., 26, 2719–2740, https://doi.org/10.1175/JCLI-D-12-00436.1, 2013.

Kay, J. E., Bourdages, L., Miller, N. B., Morrison, A., Yettella, V., Chepfer, H., and Eaton, B.: Evaluating and improving cloud phase in the Community Atmosphere Model version 5 using spaceborne lidar observations, Journal of Geophysical Research: Atmospheres, 121, 4162–4176, https://doi.org/10.1002/2015JD024699, 2016.

Ke, Z., Liu, X., Wu, M., Shan, Y., and Shi, Y.: Improved Dust Representation and Impacts on Dust Transport and Radiative Effect in CAM5, J. Adv. Model. Earth Syst., 14, e2021MS002845, https://doi.org/10.1029/2021MS002845, 2022.

Khairoutdinov, M. and Kogan, Y.: A New Cloud Physics Parameterization in a Large-Eddy Simulation Model of Marine Stratocumulus, Mon. Weather Rev., 128, 229–243, https://doi.org/10.1175/1520-0493(2000)128<0229:ANCPPI>2.0.CO;2, 2000.

King, M. D., Platnick, S., Menzel, W. P., Ackerman, S. A., and Hubanks, P. A.: Spatial and Temporal Distribution of Clouds Observed by MODIS Onboard the Terra and Aqua Satellites, IEEE Transactions on Geoscience and Remote Sensing, 51, 3826–3852, https://doi.org/10.1109/TGRS.2012.2227333, 2013.

Köhler, H.: The nucleus in and the growth of hygroscopic droplets, Trans. Faraday Soc., 32, 1152–1161, https://doi.org/10.1039/TF9363201152, 1936.

Kooperman, G. J., Pritchard, M. S., Ghan, S. J., Wang, M., Somerville, R. C. J., and Russell, L. M.: Constraining the influence of natural variability to improve estimates of global aerosol indirect effects in a nudged version of the Community Atmosphere Model 5, Journal of Geophysical Research: Atmospheres, 117, 23204, https://doi.org/10.1029/2012JD018588, 2012.

Kulmala, M., Laaksonen, A., and Pirjola, L.: Parameterizations for sulfuric acid/water nucleation rates, Journal of Geophysical Research: Atmospheres, 103, 8301–8307, https://doi.org/10.1029/97JD03718, 1998.

Langton, T., Stier, P., Watson-Parris, D., and Mulcahy, J. P.: Decomposing Effective Radiative Forcing Due to Aerosol Cloud Interactions by Global Cloud Regimes, Geophys. Res. Lett., 48, e2021GL093833, https://doi.org/10.1029/2021GL093833, 2021.

Lewis, R. and Schwartz, E.: Sea Salt Aerosol Production: Mechanisms, Methods, Measurements and Models—A Critical Review, American Geophysical Union, Washington, D. C., https://doi.org/10.1029/GM152, 2004.

Li, J., Wong, J. G. D., Dobbie, J. S., and Chýlek, P.: Parameterization of the Optical Properties of Sulfate Aerosols, J. Atmos. Sci., 58, 193–209, https://doi.org/10.1175/1520-0469(2001)058<0193:POTOPO>2.0.CO;2, 2001.

Li, J., Ma, X., von Salzen, K., and Dobbie, S.: Parameterization of sea-salt optical properties and physics of the associated radiative forcing, Atmos. Chem. Phys., 8, 4787–4798, https://doi.org/10.5194/acp-8-4787-2008, 2008.

Li, J. -L. F., Waliser, D. E., Chen, W. -T., Guan, B., Kubar, T., Stephens, G., Ma, H. -Y., Deng, M., Donner, L., Seman, C., and Horowitz, L.: An observationally based evaluation of cloud ice water in CMIP3 and CMIP5 GCMs and contemporary

https://doi.org/10.5194/egusphere-2026-6624
Preprint. Discussion started: 10 November 2026
© Author(s) 2026. CC BY 4.0 License.

reanalyses using contemporary satellite data, Journal of Geophysical Research: Atmospheres, 117, n/a-n/a, https://doi.org/10.1029/2012JD017640, 2012.

Liang, Y., Wang, L., Zhang, G. J., and Wu, Q.: Sensitivity test of parameterizations of subgrid-scale orographic form drag in the NCAR CESM1, Clim. Dyn., 48, 3365–3379, https://doi.org/10.1007/s00382-016-3272-7, 2017.

Lin, J., Qian, T., Bechtold, P., Grell, G., Zhang, G. J., Zhu, P., Freitas, S. R., Barnes, H., and Han, J.: Atmospheric Convection, Atmosphere-Ocean, 60, 422–476, https://doi.org/10.1080/07055900.2022.2082915, 2022.

Lin, Y., Huang, X., Liang, Y., Qin, Y., Xu, S., Huang, W., Xu, F., Liu, L., Wang, Y., Peng, Y., Wang, L., Xue, W., Fu, H., Zhang, G. J., Wang, B., Li, R., Zhang, C., Lu, H., Yang, K., Luo, Y., Bai, Y., Song, Z., Wang, M., Zhao, W., Zhang, F., Xu, J., Zhao, X., Lu, C., Chen, Y., Luo, Y., Hu, Y., Tang, Q., Chen, D., Yang, G., and Gong, P.: Community Integrated Earth System Model (CIESM): Description and Evaluation, J. Adv. Model. Earth Syst., 12, https://doi.org/10.1029/2019MS002036, 2020.

Liu, L., Zhang, C., Li, R., Wang, B., and Yang, G.: C-Coupler2: a flexible and user-friendly community coupler for model coupling and nesting, Geosci. Model Dev., 11, 3557–3586, https://doi.org/10.5194/gmd-11-3557-2018, 2018.

Liu, X., Penner, J. E., Ghan, S. J., and Wang, M.: Inclusion of Ice Microphysics in the NCAR Community Atmospheric Model Version 3 (CAM3), J. Clim., 20, 4526–4547, https://doi.org/10.1175/JCLI4264.1, 2007.

Liu, X., Easter, R. C., Ghan, S. J., Zaveri, R., Rasch, P., Shi, X., Lamarque, J.-F., Gettelman, A., Morrison, H., Vitt, F., Conley, A., Park, S., Neale, R., Hannay, C., Ekman, A. M. L., Hess, P., Mahowald, N., Collins, W., Iacono, M. J., Bretherton, C. S., Flanner, M. G., and Mitchell, D.: Toward a minimal representation of aerosols in climate models: description and evaluation in the Community Atmosphere Model CAM5, Geosci. Model Dev., 5, 709–739, https://doi.org/10.5194/gmd-5-709-2012, 2012.

Loeb, N. G., Wielicki, B. A., Doelling, D. R., Smith, G. L., Keyes, D. F., Kato, S., Manalo-Smith, N., and Wong, T.: Toward Optimal Closure of the Earth's Top-of-Atmosphere Radiation Budget, J. Clim., 22, 748–766, https://doi.org/10.1175/2008JCLI2637.1, 2009.

Loeb, N. G., Doelling, D. R., Wang, H., Su, W., Nguyen, C., Corbett, J. G., Liang, L., Mitrescu, C., Rose, F. G., and Kato, S.: Clouds and the Earth's Radiant Energy System (CERES) Energy Balanced and Filled (EBAF) Top-of-Atmosphere (TOA) Edition-4.0 Data Product, J. Clim., 31, 895–918, https://doi.org/10.1175/JCLI-D-17-0208.1, 2018.

Lüpkes, C., Gryanik, V. M., Hartmann, J., and Andreas, E. L.: A parametrization, based on sea ice morphology, of the neutral atmospheric drag coefficients for weather prediction and climate models, Journal of Geophysical Research: Atmospheres, 117, 13112, https://doi.org/10.1029/2012JD017630, 2012.

Ma, X., von Salzen, K., and Li, J.: Modelling sea salt aerosol and its direct and indirect effects on climate, Atmos. Chem. Phys., 8, 1311–1327, https://doi.org/10.5194/acp-8-1311-2008, 2008.

Mahowald, N. M., Muhs, D. R., Levis, S., Rasch, P. J., Yoshioka, M., Zender, C. S., and Luo, C.: Change in atmospheric mineral aerosols in response to climate: Last glacial period, preindustrial, modern, and doubled carbon dioxide climates, Journal of Geophysical Research: Atmospheres, 111, https://doi.org/10.1029/2005JD006653, 2006a.

https://doi.org/10.5194/egusphere-2026-6624
Preprint. Discussion started: 10 November 2026
© Author(s) 2026. CC BY 4.0 License.

Mahowald, N. M., Yoshioka, M., Collins, W. D., Conley, A. J., Fillmore, D. W., and Coleman, D. B.: Climate response and radiative forcing from mineral aerosols during the last glacial maximum, pre-industrial, current and doubled-carbon dioxide climates, Geophys. Res. Lett., 33, https://doi.org/10.1029/2006GL026126, 2006b.

Mårtensson, E. M., Nilsson, E. D., de Leeuw, G., Cohen, L. H., and Hansson, H. -C.: Laboratory simulations and parameterization of the primary marine aerosol production, Journal of Geophysical Research: Atmospheres, 108, n/a-n/a, https://doi.org/10.1029/2002JD002263, 2003.

Matus, A. V. and L'Ecuyer, T. S.: The role of cloud phase in Earth's radiation budget, Journal of Geophysical Research: Atmospheres, 122, 2559–2578, https://doi.org/10.1002/2016JD025951, 2017.

McCoy, I. L., McCoy, D. T., Wood, R., Regayre, L., Watson-Parris, D., Grosvenor, D. P., Mulcahy, J. P., Hu, Y., Bender, F. A.-M., Field, P. R., Carslaw, K. S., and Gordon, H.: The hemispheric contrast in cloud microphysical properties constrains aerosol forcing, Proceedings of the National Academy of Sciences, 117, 18998–19006, https://doi.org/10.1073/pnas.1922502117, 2020.

Merikanto, J., Napari, I., Vehkamäki, H., Anttila, T., and Kulmala, M.: New parameterization of sulfuric acid-ammonia-water ternary nucleation rates at tropospheric conditions, Journal of Geophysical Research: Atmospheres, 112, 15207, https://doi.org/10.1029/2006JD007977, 2007.

Mlawer, E. J., Taubman, S. J., Brown, P. D., Iacono, M. J., and Clough, S. A.: Radiative transfer for inhomogeneous atmospheres: RRTM, a validated correlated-k model for the longwave, Journal of Geophysical Research: Atmospheres, 102, 16663–16682, https://doi.org/10.1029/97JD00237, 1997.

Monahan, E. C., Spiel, D. E., and Davidson, K. L.: A Model of Marine Aerosol Generation Via Whitecaps and Wave Disruption, American Meteorological Soc, 167–174, https://doi.org/10.1007/978-94-009-4668-2_16, 1986.

Morrison, H. and Gettelman, A.: A New Two-Moment Bulk Stratiform Cloud Microphysics Scheme in the Community Atmosphere Model, Version 3 (CAM3). Part I: Description and Numerical Tests, J. Clim., 21, 3642–3659, https://doi.org/10.1175/2008JCLI2105.1, 2008.

Mülmenstädt, J., Gryspeerdt, E., Salzmann, M., Ma, P.-L., Dipu, S., and Quaas, J.: Separating radiative forcing by aerosol–cloud interactions and rapid cloud adjustments in the ECHAM–HAMMOZ aerosol–climate model using the method of partial radiative perturbations, Atmos. Chem. Phys., 19, 15415–15429, https://doi.org/10.5194/acp-19-15415-2019, 2019.

Myhre, G., Samset, B. H., Schulz, M., Balkanski, Y., Bauer, S., Berntsen, T. K., Bian, H., Bellouin, N., Chin, M., Diehl, T., Easter, R. C., Feichter, J., Ghan, S. J., Hauglustaine, D., Iversen, T., Kinne, S., Kirkevåg, A., Lamarque, J.-F., Lin, G., Liu, X., Lund, M. T., Luo, G., Ma, X., van Noije, T., Penner, J. E., Rasch, P. J., Ruiz, A., Seland, Ø., Skeie, R. B., Stier, P., Takemura, T., Tsigaridis, K., Wang, P., Wang, Z., Xu, L., Yu, H., Yu, F., Yoon, J.-H., Zhang, K., Zhang, H., and Zhou, C.: Radiative forcing of the direct aerosol effect from AeroCom Phase II simulations, Atmos. Chem. Phys., 13, 1853–1877, https://doi.org/10.5194/acp-13-1853-2013, 2013.

Myhre, G., Aas, W., Cherian, R., Collins, W., Faluvegi, G., Flanner, M., Forster, P., Hodnebrog, Ø., Klimont, Z., Lund, M. T., Mülmenstädt, J., Lund Myhre, C., Olivié, D., Prather, M., Quaas, J., Samset, B. H., Schnell, J. L., Schulz, M., Shindell, D.,

https://doi.org/10.5194/egusphere-2026-6624
Preprint. Discussion started: 10 November 2026
© Author(s) 2026. CC BY 4.0 License.

Skeie, R. B., Takemura, T., and Tsyro, S.: Multi-model simulations of aerosol and ozone radiative forcing due to anthropogenic emission changes during the period 1990–2015, Atmos. Chem. Phys., 17, 2709–2720, https://doi.org/10.5194/acp-17-2709-2017, 2017.

Nakajima, T. and King, M. D.: Determination of the Optical Thickness and Effective Particle Radius of Clouds from Reflected Solar Radiation Measurements. Part I: Theory, J. Atmos. Sci., 47, 1878–1893, https://doi.org/10.1175/1520-0469(1990)047<1878:DOTOTA>2.0.CO;2, 1990.

Neale, R. B., Gettelman, A., Park, S., Chen, C.-C., Lauritzen, P. H., Williamson, D. L., Conley, A. J., Kinnison, D., Marsh, D., Smith, A. K., Vitt, F. M., Garcia, R., Lamarque, J.-F., Mills, M. J., Tilmes, S., Morrison, H., Cameron-Smith, P., Collins, W. D., Iacono, M. J., Easter, R. C., Liu, X., Ghan, S. J., Rasch, P. J., and Taylor, M. A.: Description of the NCAR Community Atmosphere Model (CAM 5.0), https://doi.org/10.5065/WGTK-4G06, 2012.

Neubauer, D., Ferrachat, S., Siegenthaler-Le Drian, C., Stier, P., Partridge, D. G., Tegen, I., Bey, I., Stanelle, T., Kokkola, H., and Lohmann, U.: The global aerosol–climate model ECHAM6.3–HAM2.3 – Part 2: Cloud evaluation, aerosol radiative forcing, and climate sensitivity, Geosci. Model Dev., 12, 3609–3639, https://doi.org/10.5194/gmd-12-3609-2019, 2019.

Di Noia, A., Hasekamp, O. P., van Diedenhoven, B., and Zhang, Z.: Retrieval of liquid water cloud properties from POLDER-3 measurements using a neural network ensemble approach, Atmos. Meas. Tech., 12, 1697–1716, https://doi.org/10.5194/amt-12-1697-2019, 2019.

Okin, G. S.: A new model of wind erosion in the presence of vegetation, J. Geophys. Res. Earth Surf., 113, 2–10, https://doi.org/10.1029/2007JF000758, 2008.

Painemal, D. and Zuidema, P.: Assessment of MODIS cloud effective radius and optical thickness retrievals over the Southeast Pacific with VOCALS-REx in situ measurements, Journal of Geophysical Research: Atmospheres, 116, n/a-n/a, https://doi.org/10.1029/2011JD016155, 2011.

Peng, Y., Lohmann, U., Leaitch, R., Banic, C., and Couture, M.: The cloud albedo-cloud droplet effective radius relationship for clean and polluted clouds from RACE and FIRE.ACE, Journal of Geophysical Research: Atmospheres, 107, AAC 1-1-AAC 1-6, https://doi.org/10.1029/2000JD000281, 2002.

Peng, Y., von Salzen, K., and Li, J.: Simulation of mineral dust aerosol with Piecewise Log-normal Approximation (PLA) in CanAM4-PAM, Atmos. Chem. Phys., 12, 6891–6914, https://doi.org/10.5194/acp-12-6891-2012, 2012.

Peters, D. M., Grainger, R. G., and Thomas, G.: Aerosol optical properties, in: DLR Forschungsberichte, 222–226, 2010.

Petters, M. D. and Kreidenweis, S. M.: A single parameter representation of hygroscopic growth and cloud condensation nucleus activity, Atmos. Chem. Phys., 7, 1961–1971, https://doi.org/10.5194/acp-7-1961-2007, 2007.

Pierce, J. R. and Adams, P. J.: Uncertainty in global CCN concentrations from uncertain aerosol nucleation and primary emission rates, Atmos. Chem. Phys., 9, 1339–1356, https://doi.org/10.5194/acp-9-1339-2009, 2009.

Pincus, R., Hubanks, P. A., Platnick, S., Meyer, K., Holz, R. E., Botambekov, D., and Wall, C. J.: Updated observations of clouds by MODIS for global model assessment, Earth Syst. Sci. Data, 15, 2483–2497, https://doi.org/10.5194/essd-15-2483-2023, 2023.

https://doi.org/10.5194/egusphere-2026-6624
Preprint. Discussion started: 10 November 2026
© Author(s) 2026. CC BY 4.0 License.

Platnick, S., King, M. D., Ackerman, S. A., Menzel, W. P., Baum, B. A., Riedi, J. C., and Frey, R. A.: The MODIS cloud products: algorithms and examples from terra, IEEE Transactions on Geoscience and Remote Sensing, 41, 459–473, https://doi.org/10.1109/TGRS.2002.808301, 2003.

Pöschl, U., Canagaratna, M., Jayne, J. T., Molina, L. T., Worsnop, D. R., Kolb, C. E., and Molina, M. J.: Mass Accommodation Coefficient of H2SO4 Vapor on Aqueous Sulfuric Acid Surfaces and Gaseous Diffusion Coefficient of H2SO4 in N2/H2O, J. Phys. Chem. A, 102, 10082–10089, https://doi.org/10.1021/jp982809s, 1998.

Qin, Y., Lin, Y., Xu, S., Ma, H., and Xie, S.: A Diagnostic PDF Cloud Scheme to Improve Subtropical Low Clouds in NCAR Community Atmosphere Model (CAM5), J. Adv. Model. Earth Syst., 10, 320–341, https://doi.org/10.1002/2017MS001095, 2018.

Quaas, J. and Gryspeerdt, E.: Aerosol-cloud interactions in liquid clouds, in: Aerosols and Climate, vol. 13, Elsevier, 489–544, https://doi.org/10.1016/B978-0-12-819766-0.00019-5, 2022.

Quaas, J., Boucher, O., and Lohmann, U.: Constraining the total aerosol indirect effect in the LMDZ and ECHAM4 GCMs using MODIS satellite data, Atmos. Chem. Phys., 6, 947–955, https://doi.org/10.5194/acp-6-947-2006, 2006.

Quaas, J., Boucher, O., Bellouin, N., and Kinne, S.: Satellite-based estimate of the direct and indirect aerosol climate forcing, Journal of Geophysical Research: Atmospheres, 113, 5204, https://doi.org/10.1029/2007JD008962, 2008.

Rasch, P. J., Barth, M. C., Kiehl, J. T., Schwartz, S. E., and Benkovitz, C. M.: A description of the global sulfur cycle and its controlling processes in the National Center for Atmospheric Research Community Climate Model, Version 3, Journal of Geophysical Research: Atmospheres, 105, 1367–1385, https://doi.org/10.1029/1999JD900777, 2000.

Rosenfeld, D., Wang, H., and Rasch, P. J.: The roles of cloud drop effective radius and LWP in determining rain properties in marine stratocumulus, Geophys. Res. Lett., 39, 2012, https://doi.org/10.1029/2012GL052028, 2012.

Rossow, W. B. and Schiffer, R. A.: ISCCP Cloud Data Products, Bull. Am. Meteorol. Soc., 72, 2–20, https://doi.org/10.1175/1520-0477(1991)072<0002:ICDP>2.0.CO;2, 1991.

Russell, L. M., Pandis, S. N., and Seinfeld, J. H.: Aerosol production and growth in the marine boundary layer, Journal of Geophysical Research: Atmospheres, 99, 20989–21003, https://doi.org/10.1029/94JD01932, 1994.

von Salzen, K.: Piecewise log-normal approximation of size distributions for aerosol modelling, Atmos. Chem. Phys., 6, 1351–1372, https://doi.org/10.5194/acp-6-1351-2006, 2006.

von Salzen, K., Leighton, H. G., Ariya, P. A., Barrie, L. A., Gong, S. L., Blanchet, J. -P., Spacek, L., Lohmann, U., and Kleinman, L. I.: Sensitivity of sulphate aerosol size distributions and CCN concentrations over North America to SOx emissions and H2O2 concentrations, Journal of Geophysical Research: Atmospheres, 105, 9741–9765, https://doi.org/10.1029/2000JD900027, 2000.

von Salzen, K., Whaley, C. H., Anenberg, S. C., Van Dingenen, R., Klimont, Z., Flanner, M. G., Mahmood, R., Arnold, S. R., Beagley, S., Chien, R.-Y., Christensen, J. H., Eckhardt, S., Ekman, A. M. L., Evangeliou, N., Faluvegi, G., Fu, J. S., Gauss, M., Gong, W., Hjorth, J. L., Im, U., Krishnan, S., Kupiainen, K., Kühn, T., Langner, J., Law, K. S., Marelle, L., Olivié, D., Onishi, T., Oshima, N., Paunu, V.-V., Peng, Y., Plummer, D., Pozzoli, L., Rao, S., Raut, J.-C., Sand, M., Schmale, J., Sigmond,

© Author(s) 2026. CC BY 4.0 License.

M., Thomas, M. A., Tsigaridis, K., Tsyro, S., Turnock, S. T., Wang, M., and Winter, B.: Clean air policies are key for successfully mitigating Arctic warming, Commun. Earth Environ., 3, 222, https://doi.org/10.1038/s43247-022-00555-x, 2022.

Schmale, J., Henning, S., Henzing, B., Keskinen, H., Sellegri, K., Ovadnevaite, J., Bougiatioti, A., Kalivitis, N., Stavroulas, I., Jefferson, A., Park, M., Schlag, P., Kristensson, A., Iwamoto, Y., Pringle, K., Reddington, C., Aalto, P., Äijälä, M., Baltensperger, U., Bialek, J., Birmili, W., Bukowiecki, N., Ehn, M., Fjæraa, A. M., Fiebig, M., Frank, G., Fröhlich, R., Frumau, A., Furuya, M., Hammer, E., Heikkinen, L., Herrmann, E., Holzinger, R., Hyono, H., Kanakidou, M., Kiendler-Scharr, A., Kinouchi, K., Kos, G., Kulmala, M., Mihalopoulos, N., Motos, G., Nenes, A., O'Dowd, C., Paramonov, M., Petäjä, T., Picard, D., Poulain, L., Prévôt, A. S. H., Slowik, J., Sonntag, A., Swietlicki, E., Svenningsson, B., Tsurumaru, H., Wiedensohler, A., Wittbom, C., Ogren, J. A., Matsuki, A., Yum, S. S., Myhre, C. L., Carslaw, K., Stratmann, F., and Gysel, M.: Collocated observations of cloud condensation nuclei, particle size distributions, and chemical composition, Sci. Data, 4, 170003, https://doi.org/10.1038/sdata.2017.3, 2017.

Schmidt, A., Carslaw, K. S., Mann, G. W., Rap, A., Pringle, K. J., Spracklen, D. V., Wilson, M., and Forster, P. M.: Importance of tropospheric volcanic aerosol for indirect radiative forcing of climate, Atmos. Chem. Phys., 12, 7321–7339, https://doi.org/10.5194/acp-12-7321-2012, 2012.

Scott, B. C.: Parameterization of Sulfate Removal by Precipitation, Journal of Applied Meteorology, 17, 1375–1389, https://doi.org/10.1175/1520-0450(1978)017<1375:POSRBP>2.0.CO;2, 1978.

Seinfeld, J. H. and Pandis, S. N.: Atmospheric Chemistry and Physics：From Air Pollution to Climate Change, 2nd edition., John Wiley & Sons Inc, 2006.

Shang, H., Letu, H., Bréon, F.-M., Riedi, J., Ma, R., Wang, Z., Nakajima, T. Y., Wang, Z., and Chen, L.: An improved algorithm of cloud droplet size distribution from POLDER polarized measurements, Remote Sens. Environ., 228, 61–74, https://doi.org/10.1016/j.rse.2019.04.013, 2019.

Shangguan, W., Dai, Y., Duan, Q., Liu, B., and Yuan, H.: A global soil data set for earth system modeling, J. Adv. Model. Earth Syst., 6, 249–263, https://doi.org/10.1002/2013MS000293, 2014.

Shi, X., Liu, X., and Zhang, K.: Effects of pre-existing ice crystals on cirrus clouds and comparison between different ice nucleation parameterizations with the Community Atmosphere Model (CAM5), Atmos. Chem. Phys., 15, 1503–1520, https://doi.org/10.5194/acp-15-1503-2015, 2015.

Song, X. and Zhang, G. J.: Microphysics parameterization for convective clouds in a global climate model: Description and single-column model tests, J. Geophys. Res., 116, D02201, https://doi.org/10.1029/2010JD014833, 2011.

Stephens, G. L., Vane, D. G., Boain, R. J., Mace, G. G., Sassen, K., Wang, Z., Illingworth, A. J., O'connor, E. J., Rossow, W. B., Durden, S. L., Miller, S. D., Austin, R. T., Benedetti, A., and Mitrescu, C.: THE CLOUDSAT MISSION AND THE A-TRAIN, Bull. Am. Meteorol. Soc., 83, 1771–1790, https://doi.org/10.1175/BAMS-83-12-1771, 2002.

Stevens, B. and Schwartz, S. E.: Observing and Modeling Earth's Energy Flows, Surv. Geophys., 33, 779–816, https://doi.org/10.1007/s10712-012-9184-0, 2012.

https://doi.org/10.5194/egusphere-2026-6624
Preprint. Discussion started: 10 November 2026
© Author(s) 2026. CC BY 4.0 License.

Stevens, B., Fiedler, S., Kinne, S., Peters, K., Rast, S., Müsse, J., Smith, S. J., and Mauritsen, T.: MACv2-SP: a parameterization of anthropogenic aerosol optical properties and an associated Twomey effect for use in CMIP6, Geosci. Model Dev., 10, 433–452, https://doi.org/10.5194/gmd-10-433-2017, 2017.

Storer, R. L., Zhang, G. J., and Song, X.: Effects of Convective Microphysics Parameterization on Large-Scale Cloud Hydrological Cycle and Radiative Budget in Tropical and Midlatitude Convective Regions, J. Clim., 28, 9277–9297, https://doi.org/10.1175/JCLI-D-15-0064.1, 2015.

Tie, X., Brasseur, G., Emmons, L., Horowitz, L., and Kinnison, D.: Effects of aerosols on tropospheric oxidants: A global model study, Journal of Geophysical Research: Atmospheres, 106, 22931–22964, https://doi.org/10.1029/2001JD900206, 2001.

Twomey, S.: The Influence of Pollution on the Shortwave Albedo of Clouds, J. Atmos. Sci., 34, 1149–1152, https://doi.org/10.1175/1520-0469(1977)034<1149:TIOPOT>2.0.CO;2, 1977.

Tzivion, S., Feingold, G., and Levin, Z.: An Efficient Numerical Solution to the Stochastic Collection Equation, J. Atmos. Sci., 44, 3139–3149, https://doi.org/10.1175/1520-0469(1987)044<3139:AENSTT>2.0.CO;2, 1987.

Wang, H., Zhang, M., Peng, Y., and Duan, J.: Analyzing the Characteristics of Cloud Condensation Nuclei (CCN) in Hebei, China Using Multi-Year Observation and Reanalysis Data, Atmosphere (Basel)., 13, 468, https://doi.org/10.3390/atmos13030468, 2022a.

Wang, H., Peng, Y., von Salzen, K., Yang, Y., Zhou, W., and Zhao, D.: Evaluation of a quasi-steady-state approximation of the cloud droplet growth equation (QDGE) scheme for aerosol activation in global models using multiple aircraft data over both continental and marine environments, Geosci. Model Dev., 15, 2949–2971, https://doi.org/10.5194/gmd-15-2949-2022, 2022b.

Wang, H., Peng, Y., Di Noia, A., Shang, H., Letu, H., van Diedenhoven, B., Hasekamp, O. P., Liu, Y., and Quaas, J.: Global quantification of the dispersion effect with POLDER satellite data, Nat. Commun., 16, 7087, https://doi.org/10.1038/s41467-025-62238-3, 2025a.

Wang, M., Peng, Y., and Liu, Y.: Contrasting Aerosol Effects on Long-Wave Cloud Forcing in South East Asia and Amazon Simulated With Community Atmosphere Model Version 5.3, Journal of Geophysical Research: Atmospheres, 125, https://doi.org/10.1029/2020JD032380, 2020.

Wang, X., Carslaw, K. S., Grosvenor, D. P., and Gordon, H.: Weak influence of anthropogenic emissions on aerosol, cloud, and rain in the wet season of the Amazon rainforest, Atmos. Chem. Phys., 25, 9685–9717, https://doi.org/10.5194/acp-25-9685-2025, 2025b.

Wang, Y., Zhang, G. J., and Craig, G. C.: Stochastic convective parameterization improving the simulation of tropical precipitation variability in the NCAR CAM5, Geophys. Res. Lett., 43, 6612–6619, https://doi.org/10.1002/2016GL069818, 2016.

Wexler, A. S. and Clegg, S. L.: Atmospheric aerosol models for systems including the ions H+, NH4+, Na+, SO42−, NO3−, Cl−, Br−, and H2O, Journal of Geophysical Research: Atmospheres, 107, 4207, https://doi.org/10.1029/2001JD000451, 2002.

https://doi.org/10.5194/egusphere-2026-6624
Preprint. Discussion started: 10 November 2026
© Author(s) 2026. CC BY 4.0 License.

Whaley, C. H., Mahmood, R., von Salzen, K., Winter, B., Eckhardt, S., Arnold, S., Beagley, S., Becagli, S., Chien, R.-Y., Christensen, J., Damani, S. M., Dong, X., Eleftheriadis, K., Evangeliou, N., Faluvegi, G., Flanner, M., Fu, J. S., Gauss, M., Giardi, F., Gong, W., Hjorth, J. L., Huang, L., Im, U., Kanaya, Y., Krishnan, S., Klimont, Z., Kühn, T., Langner, J., Law, K. S., Marelle, L., Massling, A., Olivié, D., Onishi, T., Oshima, N., Peng, Y., Plummer, D. A., Popovicheva, O., Pozzoli, L., Raut, J.-C., Sand, M., Saunders, L. N., Schmale, J., Sharma, S., Skeie, R. B., Skov, H., Taketani, F., Thomas, M. A., Traversi, R., Tsigaridis, K., Tsyro, S., Turnock, S., Vitale, V., Walker, K. A., Wang, M., Watson-Parris, D., and Weiss-Gibbons, T.: Model evaluation of short-lived climate forcers for the Arctic Monitoring and Assessment Programme: a multi-species, multi-model study, Atmos. Chem. Phys., 22, 5775–5828, https://doi.org/10.5194/acp-22-5775-2022, 2022.

Winker, D. M., Vaughan, M. A., Omar, A., Hu, Y., Powell, K. A., Liu, Z., Hunt, W. H., and Young, S. A.: Overview of the CALIPSO Mission and CALIOP Data Processing Algorithms, J. Atmos. Ocean. Technol., 26, 2310–2323, https://doi.org/10.1175/2009JTECHA1281.1, 2009.

Wu, M., Liu, X., Zhang, L., Wu, C., Lu, Z., Ma, P., Wang, H., Tilmes, S., Mahowald, N., Matsui, H., and Easter, R. C.: Impacts of Aerosol Dry Deposition on Black Carbon Spatial Distributions and Radiative Effects in the Community Atmosphere Model CAM5, J. Adv. Model. Earth Syst., 10, 1150–1171, https://doi.org/10.1029/2017MS001219, 2018.

Xia, Y., Yue, S., and Guo, Z.: A Neural-Network-Based Scheme for Improving Wegener–Bergeron–Findeisen Process and Its Impact on Mixed Phase Cloud, International Journal of Climatology, 46, e70254, https://doi.org/10.1002/joc.70254, 2026.

Yang, J., Lu, J., Deng, Y., Wang, Y., Lu, C., Yin, Y., Wang, Z., Jing, X., and Yang, K.: Parameterizing the Heterogeneous Liquid-Ice Mixing in Modeling Ice Growth Through the Wegener-Bergeron-Findeisen Process in CAM6, Geophys. Res. Lett., 52, e2024GL114036, https://doi.org/10.1029/2024GL114036, 2025.

Yang, K., Koike, T., Ishikawa, H., Kim, J., Li, X., Liu, H., Liu, S., Ma, Y., and Wang, J.: Turbulent Flux Transfer over Bare-Soil Surfaces: Characteristics and Parameterization, J. Appl. Meteorol. Climatol., 47, 276–290, https://doi.org/10.1175/2007JAMC1547.1, 2008.

YishuangLiang and hxmhuang: DESS-of-Tsinghua-University/CIESM: CIESM of Tsinghua University (Version v1.1.0) [Computer software]. Zenodo, https://doi.org/10.5281/zenodo.3596317, 2020.

Yu, H., Kaufman, Y. J., Chin, M., Feingold, G., Remer, L. A., Anderson, T. L., Balkanski, Y., Bellouin, N., Boucher, O., Christopher, S., DeCola, P., Kahn, R., Koch, D., Loeb, N., Reddy, M. S., Schulz, M., Takemura, T., and Zhou, M.: A review of measurement-based assessments of the aerosol direct radiative effect and forcing, Atmos. Chem. Phys., 6, 613–666, https://doi.org/10.5194/acp-6-613-2006, 2006.

Zaveri, R. A., Easter, R. C., Singh, B., Wang, H., Lu, Z., Tilmes, S., Emmons, L. K., Vitt, F., Zhang, R., Liu, X., Ghan, S. J., and Rasch, P. J.: Development and Evaluation of Chemistry-Aerosol-Climate Model CAM5-Chem-MAM7-MOSAIC: Global Atmospheric Distribution and Radiative Effects of Nitrate Aerosol, J. Adv. Model. Earth Syst., 13, e2020MS002346, https://doi.org/10.1029/2020MS002346, 2021.

Zhang, F. and Li, J.: Doubling–Adding Method for Delta-Four-Stream Spherical Harmonic Expansion Approximation in Radiative Transfer Parameterization, J. Atmos. Sci., 70, 3084–3101, https://doi.org/10.1175/JAS-D-12-0334.1, 2013.

https://doi.org/10.5194/egusphere-2026-6624
Preprint. Discussion started: 10 November 2026
© Author(s) 2026. CC BY 4.0 License.



Zhang, L., Gong, S., Padro, J., and Barrie, L.: A size-segregated particle dry deposition scheme for an atmospheric aerosol module, Atmos. Environ., 35, 549–560, https://doi.org/10.1016/S1352-2310(00)00326-5, 2001.

Zhang, R., Wang, Y., Li, Z., Wang, Z., Dickerson, R. R., Ren, X., He, H., Wang, F., Gao, Y., Chen, X., Xu, J., Cheng, Y., and Su, H.: Vertical profiles of cloud condensation nuclei number concentration and its empirical estimate from aerosol optical properties over the North China Plain, Atmos. Chem. Phys., 22, 14879–14891, https://doi.org/10.5194/acp-22-14879-2022, 2022.

Zhang, Z. and Platnick, S.: An assessment of differences between cloud effective particle radius retrievals for marine water clouds from three MODIS spectral bands, J. Geophys. Res., 116, D20215, https://doi.org/10.1029/2011JD016216, 2011.

Zhao, X., Lin, Y., Peng, Y., Wang, B., Morrison, H., and Gettelman, A.: A single ice approach using varying ice particle properties in global climate model microphysics, J. Adv. Model. Earth Syst., 9, 2138–2157, https://doi.org/10.1002/2017MS000952, 2017.

Zhu, Y., Rosenfeld, D., and Li, Z.: Under What Conditions Can We Trust Retrieved Cloud Drop Concentrations in Broken Marine Stratocumulus?, Journal of Geophysical Research: Atmospheres, 123, 8754–8767, https://doi.org/10.1029/2017JD028083, 2018.